PHYSICAL REVIEW A VOLUME 49, NUMBER 5 MAY 1994

# Low-energy-electron collisions with sodium: Elastic and inelastic scattering from the ground state

Wayne K. Trail, Michael A. Morrison,* Hsiao-Ling Zhou,† Barbara L. Whitten,‡ Klaus Bartschat,§
Keith B. MacAdam,** Terry L. Goforth,†† and David W. Norcross‡‡
*Joint Institute for Laboratory Astrophysics, University of Colorado and National Institute of Standards and Technology,*
*Boulder, Colorado 80309-0440*

(Received 16 September 1993)

The electron-Na system is the prototype for nonrelativistic scattering of a charged particle from a quasi-one-electron system. At scattering energies below several eV, *e*-Na cross sections are particularly sensitive to the exchange interaction and manifest a rich variety of near-threshold structures in various spin channels. By applying the nonperturbative coupled-channel *R*-matrix method in carefully converged calculations we have generated a comprehensive data base of accurate scattering quantities for studying these phenomena and for comparison to present and future experimental data. In particular, we examine elastic scattering and excitation of the 3*p*, 4*s*, 3*d*, and 4*p* excited states at energies from threshold to 8.6 eV. In addition to conventional integrated and differential cross sections, we consider partial cross sections for changes in the projection of the spin and orbital angular momentum of the Na valence electron, comparing results for all these quantities to experimental data where available.

PACS number(s): 34.80.Bm, 34.80.Dp, 34.80.Nz

## I. INTRODUCTION

In 1972 Moores and Norcross [1] reported four-state close-coupling calculations of cross sections for electron scattering from sodium in its ground state at energies below the ionization threshold at 5.14 eV. Their results have become the standard of comparison for experimental and theoretical determinations of integral and differential cross sections (DCS's) for elastic scattering [2–10], for the $3s \rightarrow 3p$ and $3s \rightarrow 3d$ excitations [11–17], and for the polarization of the line radiation from radiative decay of the final state [14–22].

During subsequent decades, however, experimental studies of electron–alkali-metal atom scattering moved in new directions, making new demands on theory. The most striking change has been an increased emphasis on collisions involving polarized beams and spin analysis of the final state [23–35]. For example, Hegemann *et al.* [36] have crossed beams of spin-polarized electrons and unpolarized sodium atoms and measured the polarization of the outgoing electron to determine spin-flip cross sections for elastic scattering and excitation of the $3\,^2P$ state, and McClelland, Kelley, and Celotta [27] have measured spin asymmetries for superelastic scattering from sodium atoms initially excited to the $3\,^2P$ state.

The latter experiment is one of several in which the target atoms are initially prepared (by one or more lasers) in an excited state [37–42]. Many of these experiments do not entail spin polarization or analysis: for example, Jaduszliwer and co-workers [38,39] used an atomic-beam recoil technique to measure absolute DCS's for superelastic (and inelastic) scattering from $3\,^2P$.

Many studies of scattering processes involving electrons and excited sodium atoms seek to determine information about the distribution of the initial (excited) atoms among various magnetic sublevels. The subject of orientation and alignment effects has yielded considerable insight and an often bewildering variety of parameters [37–40], and has been extensively reviewed [43–48]. This will be the subject of a later paper in the present series.

Until quite recently, theoretical work related to these more detailed and revealing experiments has been very limited. Thus, while Moores, Norcross, and Sheorey [49], in a continuation of the work of Moores and Norcross, did extract cross sections for scattering from the $3\,^2P$ state, they did not delve into orientation and alignment phenomena. One motivation for the present theoretical enterprise is to produce a data base of high-precision scattering quantities targeted primarily at these new experiments. Indeed, so advanced are experimental methods for low-energy electron scattering that one can seriously envision performing a "complete" scattering experiment: as first articulated by Bederson [50], such an experiment would yield sufficient independent quantities

---

*Permanent address: Department of Physics & Astronomy, University of Oklahoma, Norman, OK 73019-0225.

†Present address: Department of Physics & Astronomy, Georgia State University, Atlanta, GA 30303.

‡Permanent address: Physics Department, Colorado College, Colorado Springs, CO 80903.

§Permanent address: Department of Physics & Astronomy, Drake University, Des Moines, IA 50311.

**Permanent address: Department of Physics & Astronomy, University of Kentucky, Lexington, KY 40506-0055.

††Permanent address: Department of Physics, Southwestern Oklahoma State University, Weatherford, OK 73096.

‡‡Permanent address: Quantum Physics Division, National Institute of Standards and Technology.

to obtain full knowledge of all relevant scattering amplitudes [34,35].

Experiments that aspire to "completeness" often measure quantities that are far more sensitive tests of theory than are the familiar differential and integral cross sections. Consequently in the present calculations, which emphasize energies below the ionization threshold, we have sought to improve on the formulation used by Moores and Norcross in several ways—primarily through enhanced convergence, as required for the scattering quantities of current interest, and a more rigorous treatment of the target and its (induced) polarization interaction with the projectile. The theoretical approach implemented here is based on an expansion of the electron-atom wave function in bound states of the target, and so does not explicitly allow for virtual excitation of the continuum; we shall discuss the justification for this assumption in Sec. IV A 4.

This formulation is described in Secs. II and III of this, the first of several papers which report our results and discuss their implications for prior experiments and theoretical studies. As befits a foundation paper, we also discuss here the convergence criterion for our calculations. Then in Sec. IV we present differential and integral cross sections for excitation from the ground ($3\,^2S$) state, comparing primarily to data from experiments which entail neither (final) state selection nor spin polarization. In subsequent papers we shall report cross sections for elastic and inelastic scattering of sodium from the $3\,^2P$ excited state, orientation and alignment parameters for this process, and scattering of polarized electrons from the ground and $3\,^2P$ states. Unless otherwise specified we use atomic units for length ($a_0$), cross sections ($a_0^2$), and polarizabilities ($a_0^3$), where the Bohr radius is $a_0 = 5.291\,77\times10^{-11}$ m.

## II. THE SODIUM ATOM

Before summarizing our formulation of the collision problem, we first consider the representation of the target and its interaction with the projectile. Sodium is effectively hydrogenic, its neonlike $1s^22s^22p^6$ core being very tightly bound. Moreover, its nuclear charge $Z=11$ is sufficiently small that in the present study the spin-orbit interaction term in the $e$-Na Hamiltonian is negligible, because the separation between the atomic terms of Na is much larger than the fine and hyperfine splitting [51]. Although the total spin of the $e$-Na system is therefore conserved, the spin of the projectile can change via exchange with the valence electron of the target.

We can therefore accurately represent bound states of the target in the $LS$-coupling approximation, i.e., we assume that the target orbital and spin angular momentum $\hat{\mathbf{L}}$ and $\hat{\mathbf{S}}$ are constants of the motion, and label the $N_e$-electron atomic wave functions for a particular electronic configuration $\Gamma$ by quantum numbers $L$, $S$, $M_L$, and $M_S$. We construct these wave functions from one-electron orbitals calculated using the restricted Hartree-Fock (RHF) method [52,53].

In generating RHF orbitals for use in scattering calculations we treat the core and valence orbitals differently. The $1s$, $2s$, and $2p$ core orbitals we obtain by solving the target Schrödinger equation (with the HF Hamiltonian of the neutral atom) for the ground-state wave function are "frozen" in subsequent scattering calculations, in the sense that these orbitals are not allowed to respond to the electric fields of the valence electron or the projectile. Of course, the valence electron (in the ground and excited states) does polarize the core and so it experiences a potential different from that produced by these frozen orbitals. To include this effect simply and semiempirically, we determine the valence and excited orbitals via a separate calculation in which we augment the HF Hamiltonian of the target with an $l$-dependent one-electron polarization potential $V_l^{(\mathrm{pol})}(r_{N_e})$ (discussed in Sec. III B), as

$$\hat{\mathcal{H}}_l^{N_e} \equiv \sum_{i=1}^{N_e}\left[-\tfrac{1}{2}\nabla_i^2-\frac{Z}{r_i}\right]+\sum_{i>j}\frac{1}{r_{ij}}+V_l^{(\mathrm{pol})}(r_{N_e})\ , \tag{2.1}$$

where the sum runs over all $N_e$ target electrons, and $r_{N_e}$ is the radial coordinate of the valence electron. We adjust the parameters $\rho_l$ in $V_l^{(\mathrm{pol})}(r_{N_e})$ for $l=0$, 1, and 2 to ensure that the resulting orbital energies reproduce experimental ionization energies for the valence ($3s$) orbital and excited $s$, $p$, and $d$ orbitals to better than 1%.

We represent core and valence orbitals in terms of Slater-type orbitals (STO's), the parameters of which we take from Clementi and Roetti [54]. For high-lying excited states, we augment this basis with additional diffuse functions. Specifically, the target wave function $\phi_\alpha(\tau_e)$ for an atomic state $\alpha=(\Gamma,L,S,M_L,M_S)$, which depends on the spatial and spin coordinates $\tau_e$ of the $N_e=11$ bound electrons, is a linear combination of antisymmetric $N_e$-electron functions that are constructed, in turn, from one-electron orbitals. Each such $(n,l,m_l)$ spatial orbital is proportional to the spherical harmonic $Y_l^{m_l}(\hat{r})$ with radial factor $P_{nl}(r)$. The aforementioned linear combinations are eigenfunctions of the coupled orbital and spin angular momentum operators of the atom with coefficients that emerge from diagonalization of the Hamiltonian Eq. (2.1) for Na.

As detailed in an earlier paper [55], the wave functions resulting from these calculations produce oscillator strengths and an electron affinity for the $^1S^e$ state of Na$^-$ that agree very well with experimental data. The energies of the low-lying excited states we shall be considering are given (with respect to the ground state) in Table I [56]; these, of course, are the excitation thresholds for inelastic collisions.

## III. COLLISION THEORY

All of the scattering quantities we shall report in this and subsequent papers follow from $S$ matrices for the $e$-Na system. The theoretical machinery we have used to solve the Schrödinger equation for this system—the $R$-matrix method—is hence key to this work. In this section we summarize our implementation of this method, which uses the Belfast $R$-matrix codes [57–59], establishing useful notation along the way, and discuss the one nonstandard feature of our representation of the interac-

TABLE I. Thresholds of states included in *n*CC close-coupling calculations (in eV).

| State number | Valence electron | Threshold energy (eV) |
|---|---|---|
| 1 | 3*s* | 0.0 |
| 2 | 3*p* | 2.1036 |
| 3 | 4*s* | 3.1912 |
| 4 | 3*d* | 3.6168 |
| 5 | 4*p* | 3.7530 |
| 6 | 5*s* | 4.1167 |
| 7 | 4*d* | 4.2833 |
| 8 | 4*f* | 4.2881 |
| 9 | 5*p* | 4.3448 |
| 10 | 6*s* | 4.5097 |
| 11 | 5*d* | 4.5919 |
| 12 | 6*p* | 4.6243 |

tion: the polarization potential. Because of the close ties of this study to that of Moores and Norcross [1], we begin by citing briefly features of that prior work that differentiate it from the present calculations.

### A. Prior close-coupling calculations on *e*-Na

As in earlier calculations by Norcross [60], Moores and Norcross represented the sodium target with a scaled statistical model potential based on the Thomas-Fermi (TF) approximation [61]. This model includes a radial scaling factor, which determines the potential at intermediate distances, that Moores and Norcross adjusted to reproduce experimental term values—an adjustment that is crucial to ensuring, for example, correct excitation thresholds for inelastic scattering. The importance of this correction was recently confirmed by Bray, Konovalov, and McCarthy [62].

Moores and Norcross modified their TF potential to allow semiempirically for polarization of the core by the valence electron by using a one-electron polarization potential of the form $-\alpha_{\text{core}}/(r^2+r_0^2)^2$. Here $\alpha_{\text{core}}=0.884a_0^3$ is the polarizability of the $\text{Na}^+$ core [63], and the parameter $r_0$ cuts off this function at small $r$. To ensure accurate experimental energies for the $3\,^2S$ and $3\,^2P$ states, Moores and Norcross chose the value $r_0=0.6977a_0$.

In the expansion of the *e*-Na wave function in target states, they included four states: the $3\,^2D$ and $4\,^2S$ states in addition to the ground $3\,^2S$ state and the $3\,^2P$ state. (In the notation of this paper, theirs is a 4CC calculation, CC standing for close coupling.) Of these states $3\,^2P$ is the most important, since it allows for nearly all of the dipole polarizability of the (ground state) atom. Working in the *LS*-coupling approximation, Moores and Norcross solved coupled radial integrodifferential scattering equations to obtain the reactance matrix $\underline{K}$ and hence a variety of cross sections. A particularly important difference between their formulation and ours is the absence from the former of terms that model the interaction of the *two* dipole moments induced by the valence electron and the projectile, respectively (see Sec. III B).

In addition to integral and differential cross sections for elastic scattering, spin flip, and excitation of the $3\,^2P$ state (at energies up to 5 eV), Moores and Norcross calculated $P_{3p}$, the intensity of radiation that is emitted at 90° to the incident electron beam in decay of the final state [the resonance doublet $(D_2)$ line radiation]. Concerning convergence, they concluded that adding the $3\,^2D$ and $4\,^2S$ states to the target-state expansion results in only small changes in the integral elastic and $3s\rightarrow3p$ cross sections but significantly affects DCS's at some energies and angles.

In a subsequent paper, Moores, Norcross, and Sheorey [49] used reactance matrices calculated by Moores and Norcross to evaluate converged integral elastic and superelastic cross sections for scattering from an Na atom in the (excited) 3*p* state, including fine-structure transitions. At the time, however, no experimental data was available for comparison to these theoretical results.

### B. Core polarization

Before turning to the scattering problem, we here describe the differences between our treatment of core polarization and that of Moores and Norcross. At low energies, polarization of the target by the projectile is an essential part of the electron-atom interaction potential. We treat the other two parts—the static (Coulomb) potential and nonlocal exchange effects due to the antisymmetrization requirement—at the HF level in our representation of the target.

As noted in Sec. II, induced polarization of the core also plays a role in determining the orbital of the valence electron of Na. Rather than explicitly including this effect via virtual excitations of the target [64] or pseudostates, [65], we incorporate polarization semiempirically by adding to the HF Hamiltonian the operator

$$\hat{V}^{(\text{pol})}\equiv\sum_{lm}V_l^{(\text{pol})}(r)|lm\rangle\langle lm| , \tag{3.1}$$

where $V_l^{(\text{pol})}(r)$ is a semiempirical one-electron potential of the form (in rydbergs)

$$V_l^{(\text{pol})}(r)=-\frac{\alpha_{\text{core}}}{r^4}W_6(r;\rho_l) , \tag{3.2}$$

and $\alpha_{\text{core}}$ is the polarizability of the core. The cutoff function

$$W_6(r;\rho_l)\equiv1-e^{-(r/\rho_l)^6} \tag{3.3}$$

mimics the effects of short-range nonadiabatic and many-body effects that act to diminish $V_l^{(\text{pol})}(r)$ from its asymptotic value [66]. This function depends on the partial-wave order $l$ through the "cutoff radius" $\rho_l$ which, as noted in Sec. II, we choose [55] so that the Hartree-Fock eigenvalues for the valence and excited orbitals agree with the experimental ionization energies of sodium [67]. Note that this potential does not include the $r^{-6}$-dependent induced quadrupole term, the effect of which should be small for low-energy *e*-Na scattering [68]. Equation (3.2) is particularly appropriate for alkali-metal atoms, where the valence electron is sufficiently well localized outside the core that the electric field experienced by the core is nearly uniform [69].

Moreover, the flexibility of this form makes it better suited to multielectron calculations than the form used by Moores and Norcross.

In solving the scattering problem via the *R*-matrix method (Sec. III C), we also include a potential of this form in the $(N_e+1)$-electron Hamiltonian of the *e*-Na system to where it represents the additional attraction experienced by the projectile in the field of the distorted target. But to accurately represent polarization of the full system, we must also incorporate another effect. Polarization of the core by either the valence or scattering electron alters the potential experienced by the other electron. So we must allow for the interaction of the dipole moments induced by these two electrons—an effect that, for example, plays an important role in binding an extra electron to Na in the ground $(^1S)$ state of Na$^-$ [68]. In fact, calculations of the electron affinities of alkali-metal atoms have shown this "dielectronic potential" to be more important than inclusion of high-lying target states in the theory [68,70,71]. We shall investigate its importance for *e*-Na scattering in Sec. IV.

The resulting "dielectronic interaction" produces an additional $r^{-2}$ term in the off-diagonal elements of the coupling potential matrix in the integrodifferential scattering equations. We model this interaction by a phenomenological form that can be derived from classical electrostatics [72]. This "dielectronic potential," which has been widely used in bound-state calculations [73–76], depends on the coordinates of the valence electron $(\mathbf{r}_{N_e})$ and of the projectile $(\mathbf{r})$. We cut this potential off near the nucleus via a function that depends on the average $\bar{\rho}$ of the *l*-dependent cutoff radii in (3.2):

$$V^{(\mathrm{di})}(\mathbf{r},\mathbf{r}_{N_e}) = -\frac{2\alpha_{\mathrm{core}}}{r_{N_e}^2 r^2} P_1(\cos\Theta)[W_6(r;\bar{\rho})W_6(r_{N_e};\bar{\rho})]^{1/2} . \tag{3.4}$$

Note that this potential depends on the angle between the two electrons, $\cos\Theta=\hat{\mathbf{r}}\cdot\hat{\mathbf{r}}_{N_e}$, through the first-order Legendre polynomial.

The full polarization potential for the *e*-Na system, then, is the sum of one-electron potentials (3.2) for the valence and scattering electrons and the dielectronic term (3.4). This potential appears in the close-coupling equations that we solve via the *R*-matrix method—the topic of Sec. III C.

### C. The coupled-channel expansion

We base the present research on the coupled equations obtained by expanding the *e*-Na wave function in a set of channel functions that is complete in the bound-electron coordinates, which we denote collectively by $\tau_e$, and the angular and spin coordinates of the projectile, $\hat{r}$ and $\sigma$. Inserting this expansion into the $(N_e+1)$-electron Schrödinger equation and projecting out the channel functions yields the set of coupled integrodifferential radial equations we solve for the scattering matrix and thence, the cross sections.

The channel functions are eigenfunctions of the constants of the motion of the system—the total orbital and spin angular momenta and the parity—and as such are labeled by the corresponding quantum numbers $\mathcal{L}$, $\mathcal{S}$, and $\Pi$ [77]. For a particular channel $\gamma=(\alpha,l)$, corresponding to an atomic state $\alpha=(\Gamma,L,S,M_L,M_S)$ and projectile orbital angular momentum (i.e., partial wave) *l*, we construct the channel functions $\Phi_{\alpha l}^{\mathcal{S}\mathcal{L}\Pi}(\tau_e,\hat{\mathbf{r}},\sigma)$ from products of target wave functions $\phi_\alpha(\tau_e)$, spherical harmonics $Y_l^{m_l}(\hat{r})$, and spin eigenfunctions $\chi_{m_s}(\sigma)$, coupling these products to form eigenfunctions of the constants of the motion. We then expand the system wave function for a specified initial channel $\gamma_0$ in this set, thereby introducing radial channel scattering functions $F_{\gamma,\gamma_0}^{\mathcal{S}\mathcal{L}\Pi}(r)$ as

$$\Psi_{\gamma_0,E}^{\mathcal{S}\mathcal{L}\Pi}(\tau_e,\mathbf{r},\sigma)=\hat{\mathcal{A}}\frac{1}{r}\sum_{\alpha,l}\Phi_{\alpha l}^{\mathcal{S}\mathcal{L}\Pi}(\tau_e,\hat{\mathbf{r}},\sigma)F_{\alpha l,\alpha_0 l_0}^{\mathcal{S}\mathcal{L}\Pi}(r) , \tag{3.5}$$

where the bound-free antisymmetrizer $\hat{\mathcal{A}}$ ensures that the *e*-Na wave function is antisymmetric under pairwise electron interchange. Not explicitly included in this expansion are $(N_e+1)$-electron configurations constructed entirely from bound orbitals; such configurations are sometimes used to represent resonances and bound-free correlation effects [78].

The number of Na target states required in expansion (3.5) to attain convergence depends in practice on the scattering quantity being converged and on whatever independent physical variables govern this quantity (e.g., for differential cross sections, the energy and angle). We have exhaustively checked convergence of the quantities reported in Sec. IV by performing calculations using the target-state expansion shown (with their identifying monikers) in Table II. Also shown for each calculation is the range of scattering energies at which that level of expansion is required to converge the reported scattering

TABLE II. States of Na included in the close-coupling expansion. For 7CC and larger bases, the new states added to the basis in the previous row are shown in boldface. The radius of the *R*-matrix box $r_b$ is related to the extent of the largest orbital (given in parentheses). Also shown are the range of scattering energies at which we used each level of convergence.

| Calculation | Target states | $r_b$ (units of $a_0$) | $E$ (eV) |
|---|---|---|---|
| 4CC | 3*s*,3*p*,4*s*,3*d* | 34.2 (3*d*) | 0.5–8.6 |
| 7CC | 3*s*,3*p*,4*s*,3*d*,**4*p***,**4*d***,**4*f*** | 55.8 (4*f*) | 2.0–8.6 |
| 9CC | 3*s*,3*p*,4*s*,3*d*,4*p*,**5*s***,4*d*,4*f*,**5*p*** | 61.8 (5*p*) | 5.0,8.0 |
| 10CC | 3*s*,3*p*,4*s*,3*d*,4*p*,5*s*,4*d*,4*f*,5*p*,**5*d*** | 79.6 (5*d*) | 3.0–8.6 |
| 11CCa | 3*s*,3*p*,4*s*,3*d*,4*p*,5*s*,4*d*,4*f*,5*p*,**6*s***,5*d* | 79.6 (5*d*) | 4.1–4.4,5.0,8.0 |
| 11CCb | 3*s*,3*p*,4*s*,3*d*,4*p*,5*s*,4*d*,4*f*,5*p*,5*d*,**6*p*** | 89.2 (6*p*) | 4.1–4.4,5.0,8.0 |

quantities and the radius $r_b$ of the "$R$-matrix box," the (imaginary) boundary that delimits the inner region as discussed in Sec. III D. For a given $n$CC calculation, we choose this quantity to be the radius at which the amplitude of the wave function for the state with the widest spread in $r$ attains 0.001 of its maximum value. Taking full advantage of the power of the $R$-matrix method (Sec. III D) to efficiently generate scattering quantities at a large number of energies, we used a very dense energy mesh in most of these studies (these energies are indicated by solid circles on many of the graphs in Sec. IV). Complete tabulations of these results (on floppy disc) are available on request.

Far from the target, the radial functions satisfy boundary conditions that identity the reactance matrix $\underline{K}$ for scattering from initial channel $\gamma_0$ to final channel $\gamma$, i.e.,

$$F^{\mathcal{S}\mathcal{L}\Pi}_{\gamma,\gamma_0}(r) \underset{r\to\infty}{\sim} k_\gamma^{-1/2}\left[\sin\left[k_0 r - l_0\frac{\pi}{2}\right]\delta_{\gamma\gamma_0} + \cos\left[k_\gamma r - l\frac{\pi}{2}\right]K^{\mathcal{S}\mathcal{L}\Pi}_{\gamma,\gamma_0}\right], \tag{3.6}$$

where the final-state wave number $k_\gamma$ is related to the incident energy $k_0^2$, initial and final target energies, and total system energy $E$ by conservation of energy

$$E=\epsilon_{\Gamma LS}+\tfrac{1}{2}k_\gamma^2=\epsilon_{\Gamma_0 L_0 S_0}+\tfrac{1}{2}k_0^2 \ . \tag{3.7}$$

From the $K$ matrix we calculate the transition matrix

$$\underline{T}=-\frac{2i\underline{K}}{1-i\underline{K}} \ . \tag{3.8}$$

Like the $K$ matrix, $\underline{T}$ is diagonal with respect to the quantum numbers $\mathcal{S}\mathcal{L}\Pi$, and independent of the projections of the total spin and orbital angular momentum on the quantization axis and of the parity. From this matrix we can construct scattering amplitudes, differential, and total cross sections, or other scattering quantities [24,79].

The equations we must solve to obtain the $K$ matrix from the functions $F^{\mathcal{S}\mathcal{L}\Pi}_{\alpha l,\alpha_0 l_0}(r)$ are integrodifferential in nature owing to exchange terms that arise from the antisymmetrizer $\hat{\mathcal{A}}$. These equations also contain Lagrange undetermined multipliers that enforce orthogonality to bound functions $P_{nl}(r)$ of the same symmetry (same $l$). Different channel functions are coupled by the potential matrix elements

$$V^{\mathcal{S}\mathcal{L}\Pi}_{\gamma,\gamma'}(r)=\left\langle\Phi^{\mathcal{S}\mathcal{L}\Pi}_{\gamma}\left|-\frac{Z}{r}+\sum_{i=1}^{N_e}\frac{1}{|\mathbf{r}_i-\mathbf{r}|}+V_l^{(\mathrm{pol})}(r) + V^{(\mathrm{di})}(\mathbf{r},\mathbf{r}_{N_e})\right|\Phi^{\mathcal{S}\mathcal{L}\Pi}_{\gamma'}\right\rangle . \tag{3.9}$$

Unlike Moores and Norcross and many others who have studied the integrodifferential equations for $e$-Na scattering [1,80–84], we do not solve them directly. Rather, we adopt a strategy that exploits the fundamentally different physics of the electron-atom interaction near and far from the target: the $R$-matrix method.

### D. The *R*-matrix method

The $R$-matrix method [85], originally introduced to atomic physics by Burke, Hibbert, and Robb [78], has since been applied to a wide range of problems in electron-atom and -molecule scattering [86–89]. Because it is the heart of our generation of the $K$ matrices we here summarize its salient points [90], establish notation to be used here and in later papers, and report key numerical details of the present calculations [91].

The $R$-matrix method subdivides configuration space into an "inner region" (near the target) and an "outer region" (everywhere else). Near the target the (predominantly Coulomb) electron-atom interaction is strong, nonlocal exchange effects are very important, and many-electron bound-free correlation effects and nonadiabatic polarization distortions of the core must be taken into account. Outside this region, the Coulomb interaction assumes its (comparatively weak) multipolar form, exchange effects vanish, and the polarization potential reduces to a simple adiabatic form that asymptotically goes to a function whose variation with $r$ is $r^{-4}$ and that is proportional to the polarizability of the neutral atom [see Eq. (3.2)].

To acknowledge these differences between the two regions, the $R$-matrix method erects an artificial boundary between them (roughly speaking, at a value $r=r_b$, beyond which the bound orbitals are small [92] and exchange and other many-electron effects are negligible) and treats each region differently. The $R$ matrix enables us to relate the solutions in the two regions and to extract asymptotic (outer region) quantities such as the $K$ matrix that reflect the effect of the physics of the inner region. Within the "$R$-matrix box" thus constructed the (continuum) wave function of the scattering electron is represented by a linear combination of discrete basis functions in terms of which we diagonalize the $e$-Na Hamiltonian. (This diagonalization is independent of the scattering energy and so must be performed only once, a significant advantage over traditional, propagative close-coupling methods.) In the outer region, the simpler physics of the electron-target interaction reduces the coupled equations to forms that admit straightforward propagation into the asymptotic region.

Turning now to the details of the method, we begin, as before, with the $e$-Na scattering function $\Psi^{\mathcal{S}\mathcal{L}\Pi}_{\gamma_0,E}(\tau_e,\mathbf{r},\sigma)$ of Eq. (3.5). In the inner region, we shall represent the scattering electron by a linear combination of $N_b$ basis functions $\{\bar{v}_{il}(r):i=1,\ldots,N_b\}$ that are orthonormal on the interval $[0,r_b]$ and that satisfy the following boundary conditions at the boundary between the inner and outer regions [93]:

$$\left.\begin{aligned} &\bar{v}_{il}(0)=0\\ &\frac{r_b}{\bar{v}_{il}(r_b)}\frac{d}{dr}\bar{v}_{il}(r)\Big|_{r=r_b}=b \end{aligned}\right\} i=1,\ldots,N_b \ , \tag{3.10}$$

where $b$, although in principle arbitrary, is usually chosen to be zero.

We calculate the basis functions $\bar{v}_{il}(r)$ by solving uncoupled radial scattering equations using a reference potential $V^{(\mathrm{ref})}(r)$ that builds into the basis as much of the physics of the inner region as feasible, thereby reducing the number of such functions required to converge the $R$ matrix. This equation

$$\left[\frac{d^2}{dr^2}-\frac{l(l+1)}{r^2}+V^{(\mathrm{ref})}(r)+k_i^2\right]\bar{v}_{il}(r)=\sum_n \lambda_{in}^{(l)}P_{nl}(r) \tag{3.11}$$

contains Lagrange undetermined multipliers $\{\lambda_{in}^{(l)};n=l+1,\dots,n_{\max}(l)\}$ that ensure orthogonality of the basis functions to the bound radial functions of the same symmetry on $[0,r_b]$; this guarantees the correct nodal structure in the inner region. As the reference potential we use the static $e$-Na potential for the ground state $\alpha_0=3\,^2S$:

$$\begin{aligned}V^{(\mathrm{ref})}(r)&=V^{(\mathrm{st})}(r)\\&=\left\langle\phi_{\alpha_0}(\tau_e)\left|-\frac{Z}{r}+\sum_{i=1}^{N_e}\frac{1}{|\mathbf{r}_i-\mathbf{r}|}\right|\phi_{\alpha_0}(\tau_e)\right\rangle .\end{aligned} \tag{3.12}$$

The solutions of (3.11) together with the bound radial functions $P_{nl}(r)$ constitute a complete set for $[0,r_b]$ and hence a suitable basis for construction of the radial scattering function.

We form $N_b$ such functions for each channel $\gamma$ as

$$\bar{F}_{\gamma lk}^{\mathcal{S}\mathcal{L}\Pi}(r)=\sum_{i=1}^{N_b}c_{ki}^{\gamma}\bar{v}_{il}(r),\quad k=1,\dots,N_b . \tag{3.13}$$

Since the basis functions satisfy the boundary conditions (3.10), so do these linear combinations and so do the newly constructed $N_b$ $e$-Na wave functions in the inner region:

$$\bar{\Psi}_k^{\mathcal{S}\mathcal{L}\Pi}(\tau_e,\mathbf{r},\sigma)=\hat{\mathcal{A}}\frac{1}{r}\sum_{\alpha,l}\Phi_{\alpha l}^{\mathcal{S}\mathcal{L}\Pi}(\tau_e,\hat{\mathbf{r}},\sigma)\bar{F}_{\alpha lk}^{\mathcal{S}\mathcal{L}\Pi}(r) ,\quad 0\le r\le r_b , \tag{3.14}$$

where $\sigma$ is the spin coordinate of the scattering electron. We determine the expansion coefficients in (3.13), the only parts of the scattering functions $\bar{F}_{\alpha lk}^{\mathcal{S}\mathcal{L}\Pi}(r)$ not already specified, by diagonalizing the $(N_e+1)$-electron Hamiltonian in the interval $[0,r_b]$. (As we shall demonstrate at the end of this subsection, we need not include exchange terms for high-order partial waves.)

In effect, then, by imposing the boundary conditions (3.10) the $R$-matrix method transforms the continuum problem into a discrete problem that we can solve using the linear variational method. The only glitch is that this Hamiltonian is Hermitian on the infinite interval $[0,\infty]$, not on $[0,r_b]$. So to ensure that the eigenvalues we obtain by diagonalizing on the finite interval are real, we diagonalize the sum of the Hamiltonian and the Bloch operator [94]

$$\hat{\mathcal{L}}_b=\sum_{\gamma}|\Phi_{\gamma}^{\mathcal{S}\mathcal{L}\Pi}\rangle\tfrac{1}{2}\delta(r-r_b)\left[\frac{d}{dr}-\frac{b}{r}\right]\langle\Phi_{\gamma}^{\mathcal{S}\mathcal{L}\Pi}| , \tag{3.15}$$

where the sum of projection operators onto the channel subspace ensures that this operator affects only the radial coordinate of the projectile, the $\delta$ function ensures that it acts only at the boundary, and the boundary conditions (3.10) ensure Hermiticity. The constant $b$ in Eq. (3.15) is the (arbitrary) value of the logarithmic derivative of the wave function at the boundary $r_b$.

This diagonalization yields $N_b$ eigenvalues $\bar{E}_k$ and corresponding eigenvectors $\{c_{ki}^{\gamma}:k=1,\dots,N_b\}$ that, in turn, define $N_b$ discrete $e$-Na wave functions (3.14). These functions thus correspond to quantized eigenvalues that, in general, do not equal the desired total energy $E$. So to produce an approximation to the $e$-Na wave function at this energy for $0\le r\le r_b$, we must further construct linear combinations of these functions as

$$\Psi_{\gamma_0,E}^{\mathcal{S}\mathcal{L}\Pi}(\tau_e,\mathbf{r},\sigma)=\sum_{k=1}^{N_b}A_{Ek}\bar{\Psi}_k^{\mathcal{S}\mathcal{L}\Pi}(\tau_e,\mathbf{r},\sigma) . \tag{3.16}$$

The expansion coefficients $\{A_{Ek}:k=1,\dots,N_b\}$, sensibly, depend on the values of the discretized radial functions $\bar{F}_{\alpha lk}^{\mathcal{S}\mathcal{L}\Pi}(r)$, on the continuum scattering functions $F_{\alpha l,\alpha_0 l_0}^{\mathcal{S}\mathcal{L}\Pi}(r)$ at the boundary, and on the eigenvalues $\bar{E}_k$ [78]:

$$\begin{aligned}A_{Ek}&=\frac{1}{2r_b(\bar{E}_k-E)}\\&\quad\times\sum_{\gamma}\bar{F}_{\gamma k}^{\mathcal{S}\mathcal{L}\Pi}(r_b)\left[\left[r_b\frac{d}{dr}-b\right]\Phi_{\gamma,\gamma_0}^{\mathcal{S}\mathcal{L}\Pi}\right]_{r=r_b} .\end{aligned} \tag{3.17}$$

Equation (3.16) reveals the essential difference between the $R$-matrix and coupled-channel approaches to the inner region. In the latter approach, the numerical radial functions $F_{\gamma,\gamma_0}^{\mathcal{S}\mathcal{L}\Pi}(r)$ contain information about scattering of the projectile at energy $E$ from the target in initial state $\gamma_0$. In the former, this information is contained in the coefficients (3.17) that combine the discrete functions $\bar{F}_{\gamma k}^{\mathcal{S}\mathcal{L}\Pi}(r)$ into an approximate scattering function for energy $E$. Specification of the initial state is left in the $R$-matrix method to the treatment of the outer region, where the asymptotic boundary conditions (3.6) are imposed so as to yield the $K$ matrix.

However, in practice we do not need the continuum wave function to determine the $K$ matrix. We need only the $R$ matrix. By definition, the elements of this matrix relate the radial scattering functions $F_{\gamma,\gamma_0}^{\mathcal{S}\mathcal{L}\Pi}(r)$ and their first derivatives at the boundary $r=r_b$:

$$\begin{aligned}F_{\gamma,\gamma_0}^{\mathcal{S}\mathcal{L}\Pi}(r_b)&=\sum_{\gamma'}R_{\gamma\gamma'}^{\mathcal{S}\mathcal{L}\Pi}(E,r_b)\\&\quad\times\left[r\frac{d}{dr}F_{\gamma',\gamma_0}^{\mathcal{S}\mathcal{L}\Pi}(r)-bF_{\gamma',\gamma_0}^{\mathcal{S}\mathcal{L}\Pi}(r)\right]_{r=r_b} ,\end{aligned} \tag{3.18}$$

where the sum runs over all channels $\gamma=(\alpha,l)$ included in the close-coupling expansion (3.5). Given the form of the coefficients (3.17) in (3.16), the elements of the $R$ matrix can be written in terms of the discrete radial functions as

$$R^{\mathcal{S}\mathcal{L}\Pi}_{\gamma\gamma'}(E,r_b)=\frac{1}{2r_b}\sum_{k=1}^{N_b}\frac{\bar{F}^{\mathcal{S}\mathcal{L}\Pi}_{\gamma k}(r_b)\bar{F}^{\mathcal{S}\mathcal{L}\Pi}_{\gamma' k}(r_b)}{\bar{E}_k-E}\ . \tag{3.19}$$

So given the radial functions $\bar{F}^{\mathcal{S}\mathcal{L}\Pi}_{\gamma k}(r)$ at $r=r_b$ (conventionally called "surface amplitudes") and the eigenvalues $\bar{E}_k$ ( the poles of the $R$ matrix), we can calculate a finite approximation to $\underline{R}^{\mathcal{S}\mathcal{L}\Pi}_{\gamma\gamma'}$. Of course, the sum in (3.19) includes only as many surface amplitudes as we include functions in the basis $\{\bar{v}_{kl}(r):k=1,\ldots,N_b\}$ in (3.13). But we compensate for omission of high-energy terms in the diagonal elements $(\gamma'=\gamma)$ of the $R$ matrix using a procedure due to Buttle [95] that ensures rapid, accurate convergence of the $R$ matrix except at energies near the poles $\bar{E}_k$.

In practice, determining the number $N_b$ of basis functions $\bar{v}_{il}(r)$ required to accurately represent the continuum wave function requires considerable judgment. Too few functions leads to inaccurate results because the continuum is not well represented; too many functions make the calculation more unwieldy than it has to be and may introduce numerical errors that degrade accuracy.

As a final technical matter, we note that one can reduce the scale of the coupled-channel scattering calculations by exploiting the effect on the scattering functions $F^{\mathcal{S}\mathcal{L}\Pi}_{\alpha l,\alpha_0 l_0}(r)$ of the centrifugal barrier term in the kinetic-energy operator of the Hamiltonian. In particular, we can reduce the number of channel functions $\Phi^{\mathcal{S}\mathcal{L}\Pi}_{\alpha l}(\tau_e,\hat{\mathbf{r}},\sigma)$ that must be included in the basic expansion (3.5) to attain a desired degree of convergence, because the centrifugal term effectively "excludes" high-order partial waves from the region of the Na charge cloud. This exclusion, for example, minimizes the effect of exchange on the high-order channel scattering functions; at very high order, in fact, it significantly diminishes the effect of the static potential. That is, "low-order" partial waves are highly penetrating and must be treated accurately, both in the representation of the potential that acts on them and in the solution of their dynamical problem; "high-order" terms, by contrast, can accurately be included with simplifying approximations.

To illustrate, we consider a typical calculation with ten target states (10CC in Table II) at energies between 0.5 and 8.6 eV, where partial waves up to $l=80$ are required to converge the differential cross section. As shown in Table III, for each channel with a weak (or no) barrier, $l=0,\ldots,8$, we must include all ten target states and fully couple the static (S), exchange (E), and polarization (P) potentials. For states of larger partial wave order, however, we require fewer target states. By $l\approx 14$ the barrier has effectively eliminated measurable effects due to the exchange potential, and we need only couple these channels via the static and polarization potentials. Channels with even larger orders are subject to still weaker interactions, since their huge barriers largely exclude the channel scattering function from the region of strong *e*-Na Coulomb potential; these channels can be accurately included via the Born approximation [96,97].

TABLE III. Partial waves and target states included in the coupled-channel expansion (3.5) for a typical 10CC calculation.

| | Example: 10CC calculations | |
|---|---|---|
| Partial waves | Target states | Potential |
| $l=0,\ldots,8$ | $3s,3p,4s,3d,4p,5s,4d,4f,5p,5d$ | SEP |
| $l=9,\ldots,13$ | $3s,3p,4s,3d,4p,4d,4f$ | SEP |
| $l=14,\ldots,19$ | $3s,3p,4s,3d$ | SEP |
| $l=20,\ldots,26$ | $3s,3p,4s,3d$ | SP |
| $l=27,\ldots,80$ | Born approximation | |

The mitigating effects of the centrifugal barrier on high-order partial waves further eliminate the distinction between singlet and triplet scattering. For example, in Fig. 1 we show these cross sections for elastic scattering $(3s\rightarrow 3s)$ at 5.0 eV, and for the $3s\rightarrow 3p$ excitation at 8.0 eV; at these energies we must calculate separately singlet and triplet amplitudes for $l\leq 10$, but for higher $l$ we need determine only one: say, the singlet amplitude.

### E. Determination of the *K* matrix and diverse cross sections

Getting from the $R$ matrix to the $K$ matrix requires getting from the boundary of the inner region to the asymptotic region, i.e., to a value of $r$ where the potential is weak enough that the boundary conditions (3.6) are obtained. In the region $r>r_b$ the potential matrix elements reduce to a simple analytic form, the "long-range" limit

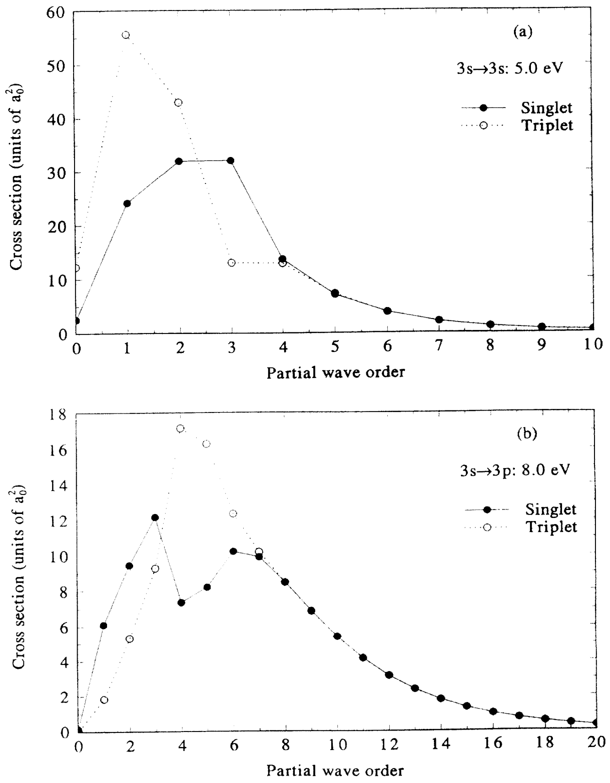

FIG. 1. Dependence of singlet (solid line and closed circles) and triplet (dotted line and open circles) *e*-Na cross sections on the number of partial waves included in Eq. (3.5). Two representative cases are plotted vs the maximum partial-wave order: (a) $3s\rightarrow 3s$ elastic scattering at 5.0 eV, and (b) the $3s\rightarrow 3p$ excitation at 8.0 eV.

of Eq. (3.9),

$$V^{\mathcal{S}\mathcal{L}\Pi}_{\gamma,\gamma'}(r) \underset{r\to\infty}{\sim} \frac{N_e}{r}\delta_{\gamma\gamma'} + \sum_{\lambda=1}^{\lambda_{\max}} \frac{1}{r^{\lambda+1}} a^{\lambda}_{\gamma\gamma'} + V_l^{(\mathrm{pol})}(r), \tag{3.20}$$

where $V_l^{(\mathrm{pol})}(r)$ is the one-electron polarization potential defined in Eq. (3.2), and the multipole matrix elements, which also include the dielectronic potential of Sec. III B, are

$$a^{\lambda}_{\gamma\gamma'} = \left\langle \Phi^{\mathcal{S}\mathcal{L}\Pi}_{\gamma} \left| \sum_{k=1}^{N_e} P_{\lambda}(\hat{r}\cdot\hat{r}_k) \left\{ r_k^{\lambda} - \frac{\alpha_{\mathrm{core}}}{r_k^2}[W_6(r_k;\bar{\rho})]^{1/2}\delta_{\lambda 1} \right\} \right| \Phi^{\mathcal{S}\mathcal{L}\Pi}_{\gamma'} \right\rangle . \tag{3.21}$$

Because the matrix elements (3.20) are not zero, we require radial functions in the outer region that satisfy coupled *differential* equations,

$$\left[ \frac{d^2}{dr^2} - \frac{l_0(l_0+1)}{r^2} + \frac{2N_e}{r} - 2V_l^{(\mathrm{pol})}(r) + k_0^2 \right] F^{\mathcal{S}\mathcal{L}\Pi}_{\gamma,\gamma_0}(r)$$

$$-2\sum_{\gamma'} \left[ \sum_{\lambda=1}^{\lambda_{\max}} \frac{1}{r^{\lambda+1}} a^{\lambda}_{\gamma\gamma'} \right] F^{\mathcal{S}\mathcal{L}\Pi}_{\gamma',\gamma_0}(r) = 0 , \tag{3.22}$$

and that reduce to the boundary conditions (3.6) as $r\to\infty$. To facilitate determination of the solution we use well-established methods of asymptotic expansion [98–100]. Specifically, we used an asymptotic package based on the variable phase method [101].

Once one has converted the $K$ matrix to a transition matrix via (3.8), one can calculate the (spin irreducible) singlet ($2\mathcal{S}+1=1$) and triplet ($2\mathcal{S}+1=3$) elastic scattering amplitudes for incident energy $E_0=k_0^2/2$ as

$${}^{2\mathcal{S}+1}f_{3s\to 3s}(\theta) = \frac{i}{2k_0} \sum_{\mathcal{L}=0}^{\infty} (2\mathcal{L}+1) P_{\mathcal{L}}(\cos\theta) T^{\mathcal{S}\mathcal{L}\Pi}_{\gamma,\gamma_0} . \tag{3.23}$$

These amplitudes are simply related to the familiar direct and exchange amplitudes by

$$f^{(d)}_{3s\to 3s}(\theta) = \tfrac{1}{2}[{}^1f_{3s\to 3s}(\theta) + {}^3f_{3s\to 3s}(\theta)] , \tag{3.24a}$$

$$f^{(e)}_{3s\to 3s}(\theta) = \tfrac{1}{2}[{}^1f_{3s\to 3s}(\theta) - {}^3f_{3s\to 3s}(\theta)] . \tag{3.24b}$$

At energies below the first inelastic threshold $\epsilon_{3p}$, we can express the singlet and triplet amplitudes Eq. (3.23) in terms of phase shifts in these spin channels as

$${}^{2\mathcal{S}+1}f_{3s\to 3s}(\theta) = \frac{1}{2ik_0} \sum_{l=0}^{\infty} (2l+1) P_l(\cos\theta) (e^{2i\,{}^{2\mathcal{S}+1}\eta_l} - 1) . \tag{3.25}$$

At all energies, we can use the singlet and triplet amplitudes to construct differential and integral cross sections [1,79]. The integral elastic cross section, for example, is simply

$$\sigma_{3s\to 3s} = \frac{\pi}{4k_0^2} \sum_{\mathcal{L}} (2\mathcal{L}+1) | T^{1\mathcal{L}\Pi}_{\alpha_0\mathcal{L},\alpha_0\mathcal{L}} + 3T^{3\mathcal{L}\Pi}_{\alpha_0\mathcal{L},\alpha_0,\mathcal{L}} |^2 , \tag{3.26}$$

where we note that both singlet and triplet scattering contribute. Similarly, we can calculate the inelastic amplitudes for excitation of the $M_L$ sublevel of the $3p$ state from the $T$ matrix as

$${}^{2\mathcal{S}+1}f_{3s,0\to 3p,M_L}(\theta) = \frac{1}{2i} \left[ \frac{4\pi}{k_0 k} \right]^{1/2} \sum_{\mathcal{L}=0}^{\infty} \sum_{l=\mathcal{L}\pm 1} i^{\mathcal{L}-l} (2\mathcal{L}+1) C(l1\mathcal{L};-M_L M_L) Y_l^{-M_L}(\theta,\varphi) T^{\mathcal{S}\mathcal{L}\Pi}_{al,\alpha_0\mathcal{L}} . \tag{3.27}$$

The squared moduli of the singlet and triplet amplitudes contribute to the differential cross section for the $3s\to 3p$ (averaged over initial and summed over final spin projections) as

$$\left.\frac{d\sigma}{d\Omega}\right|_{3s\to 3p} = \frac{k}{k_0} \sum_{M_L=-1}^{+1} [\tfrac{3}{4}|{}^3f_{3s,0\to 3p,M_L}(\theta)|^2$$

$$+ \tfrac{1}{4}|{}^1f_{3s,0\to 3p,M_L}(\theta)|^2] . \tag{3.28}$$

In discussions of near-threshold structures (as in Sec. IV) it is useful to decompose elastic and inelastic cross sections into components identified with particular partial waves—i.e., for scattering from the ground state, with particular total orbital and spin angular momenta $\mathcal{L}$ and $\mathcal{S}$. These partial cross sections are

$$\sigma^{\mathcal{L},\mathcal{S}}_{\gamma_0\to\gamma} = \frac{\pi}{k_0^2} \sum_{l_0,l} \frac{(2\mathcal{L}+1)}{(2L_0+1)} \frac{(2\mathcal{S}+1)}{(2S_0+1)} | T^{\mathcal{S}\mathcal{L}\Pi}_{\gamma,\gamma_0} |^2 , \tag{3.29}$$

where we recall that $S_0$ is the spin and $L_0$ is the angular momentum of the target in the entrance channel $\gamma_0$.

## IV. RESULTS

### A. Integrated cross sections

We begin with integrated cross sections for elastic and inelastic scattering from the ground state. These cross sections, shown in Fig. 2, manifest a remarkable diversity of structures at the various excitation thresholds throughout the energy range from 0.5 to 8.6 eV. The

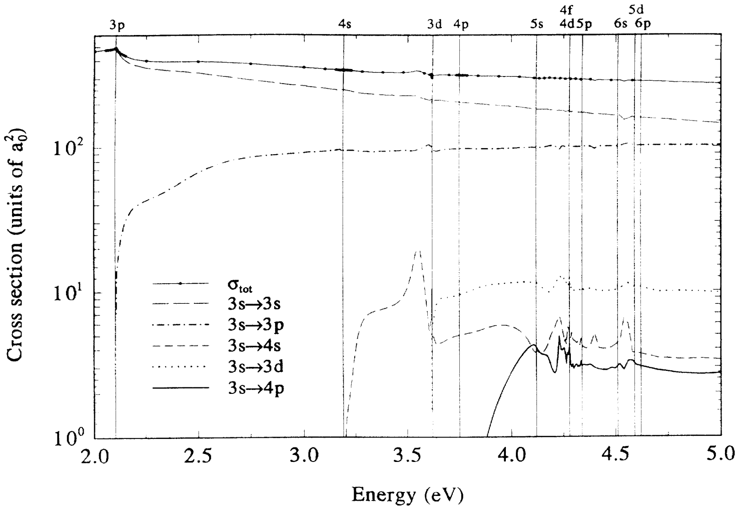

FIG. 2. Theoretical integrated total (solid line with points), $3s \rightarrow 3s$ elastic (long-dashed line), and various $3s \rightarrow nl$ inelastic *e*-Na cross sections from the present 10CC *R*-matrix calculations. The inelastic cross sections shown are those discussed in Sec. IV: $3s \rightarrow 3p$ (dot-dashed line), $3s \rightarrow 4s$ (medium-dashed line), $3s \rightarrow 3d$ (dotted line), and $3s \rightarrow 4p$ (thick solid line). Vertical lines indicate excitation thresholds (see Table I).

sum of cross sections for all energetically allowed scattering processes at a given energy is the total cross section in this figure:

$$\sigma_{\text{tot}} = \sum_{nl \geq 3s} \sigma_{3s \rightarrow nl} \; . \tag{4.1}$$

In this section we shall compare these cross sections to experimental data and discuss particularly interesting physical features of them.

### *1. Excitation of the 3p state*

The most thoroughly studied low-energy *e*-Na scattering process is the "resonance" excitation $3s \rightarrow 3p$, so called because of its exceptionally strong transition probability. Most experimental cross sections for this process have been determined from measured optical excitation functions. Enemark and Gallagher [11], for example, used crossed electron and ground-state Na beams to induce this transition. In their experiment, atoms excited by the collision subsequently decay, emitting photons at 5890 and 5896 Å (the Na *D* lines). By observing the photons emitted at 90° to the directions of the incident electron and Na beams, Enemark and Gallagher determine two quantities: the polarization of the (unresolved) doublet radiation and the *relative apparent electron excitation function*. The former is just the difference of the intensities of photons with polarizations parallel and perpendicular to the incident electron wave vector divided by the sum of these intensities (and converted to a percentage). The latter is the sum of these intensities normalized to the total electron current that passes through the target beam.

Determining integrated cross sections from optical excitation functions requires two corrections of the raw data: for cascade and for the anisotropy of polarized fluorescence [102]. These corrections alone do not place the resulting cross sections on an absolute scale. For example, Enemark and Gallagher first correct their excitation functions, then determine absolute cross sections by normalizing the shape of the results to the predictions of the first Born approximation at energies a few hundred times threshold.

Cascade corrections account for electrons in the incident beam that excite Na states above the level of interest—here, states above the 3*p* state. These higher-lying states decay to the 3*p* state and so contribute to the measured fluorescence. The experiments do not distinguish between photons resulting from direct electron-impact excitation of the 3*p* state and those from excitation to a higher-lying state (say 5*s*) followed by two-step radiative decay, first to the 3*p* and thence to the ground state. Only at energies below the next-highest excitation threshold is the measured optical excitation function actually proportional to the integrated cross section.

Because direct excitation of the 3*p* state is particularly strong, cascade corrections to the optical excitation function for this state are comparatively small: Enemark and Gallagher estimate that about 75% of this cascade comes from the 3*d* state, 5% from higher-lying *d* states, and the rest from high-lying *s* states, the most important of these being 4*s*. (Contributions from high-lying *p* states to the cascade to 3*p* are negligible.) In determining cross sections for excitation of higher-lying states, however, cascade effects are often much more important than for the 3*p* state.

Figure 3 illustrates these points in a comparison of $3s \rightarrow 3p$ cross sections from the present *R*-matrix calculations to the results of Enemark and Gallagher [11] and Phelps and Lin [14,103]. Contrasting the latter results with and without cascade correction shows the magnitude of cascade effects for this cross section. Our theoretical results from the various *n*CC close-coupling calculations listed in Table II clearly demonstrate the nature of convergence for this cross section. The 4CC results of Moores and Norcross [1] (not shown) are graphically indistinguishable from the present 4CC results, which differ in ways described in Sec. II A. At energies above 4 eV, we find the 4CC representation of the target to be inadequate: the additional higher-lying 4*p*, 4*d*, and 4*f* states included in our 7CC calculations are essential to accurately determining the *magnitude* of this cross section above a few eV. To accurately reproduce the structures at thresholds above that of the 3*d* level (3.62 eV), an even

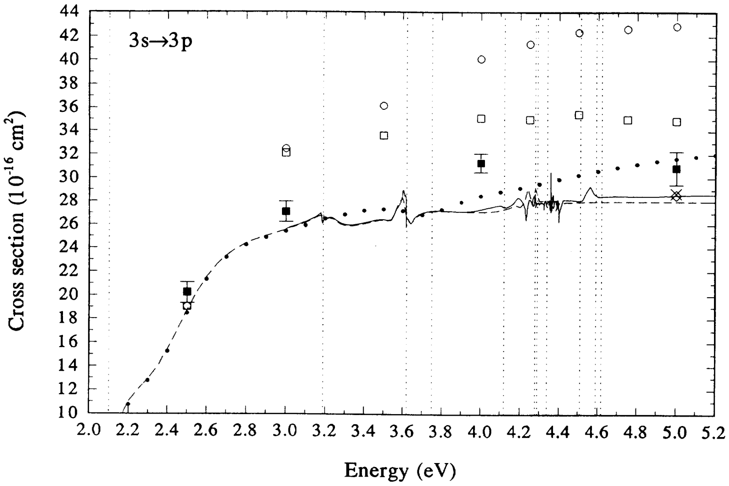

FIG. 3. Comparison of $3s \rightarrow 3p$ *e*-Na integrated cross sections to experimental data of Enemark and Gallagher (Ref. [11]) (solid boxes) and Phelps and Lin (Ref. [14]) with (open boxes) and without (open circles) cascade corrections. Theoretical results are from 11CC with 6*s* (open diamonds), 11CC with 6*p* (crosses), 10CC (solid curve), 7CC (dashed curve), and 4CC (closed circles) *R*-matrix calculations (all as described in Table II). Thresholds are shown as in Fig. 2.

more capacious representation that includes the 5*s*, 5*p*, and 5*d* states of our 10CC and 11CC calculations is required. As we shall see in subsequent subsections, these $n=4$ and 5 states are even more important for the structurally richer excitation cross sections for states above 3*p*.

Unlike Enemark and Gallagher, Phelps and Lin [14] excite their sodium atoms by passing an electron beam through a heated collision chamber filled with gas-phase Na. They too observe photons emitted at right angles to the axis of the electron beam. From this measurement at a single angle, Phelps and Lin determine the total intensity integrated over all angles (this quantity is proportional to the sum of the intensities of components of light emitted at 90° with the electric vector of the photon parallel and perpendicular to the incident electron wave vector) and thence the optical excitation function. They studied an enormous number of states over a wide range of energies, including the four lowest members of the *ns*, *np*, and *nd* manifolds from 0 to 150 eV, incorporating careful corrections for radiative cascade from higher-lying states. In Fig. 3 we show their results for the $3s \rightarrow 3p$ transition, and in subsequent sections will examine their cross sections for other transitions.

In their discussion of the earlier 4CC results of Moores and Norcross [1], Phelps and Lin note good agreement within a narrow energy range from the 3*p* threshold (2.10 eV) to 2.5 eV but "a considerable discrepancy, in both shape and magnitude, between theory and experiment" between 2.8 and 5.0 eV, where their (cascade corrected) data does not exhibit the flattening seen in the theoretical cross sections. By way of explanation, Phelps and Lin suggest that "perhaps in this region, just below the ionization threshold, the close-coupling expansion may not be fully converged with only four states." Since convergence is at issue for this excitation, we show in Fig. 4 convergence studies for the singlet and triplet parts of this cross section [104]. These studies show in more detail that although a four-state representation of the target is inadequate in this energy range, a lack of convergence for the 4CC results explains the (small) shape discrepancy, but not the magnitude discrepancy, between theory and experiment—this disagreement is, in fact, more severe for our converged (7CC, 10CC, and 11CC) results than for our 4CC results. The energy range around 4 eV is particularly rich in structures, and Fig. 4 shows the origin in the two spin channels of the various near-threshold structures evident in Fig. 3. The inset on these figures show results from the two 11CC calculations described in Table II to show that even in the region of the densest maze of near-threshold structures, the present 10CC results are converged in all but the finest detail. For example, the structure just above the 5*s* threshold at 4.21 eV is due solely to scattering in the triplet channel. Finally, we note the considerable sensitivity of some of these structures to the representation of the target, an acuteness that will be exacerbated in the higher excitations to be discussed below.

### 2. *Excitation of the 3d and 4s states*

Unlike excitation of the 3*p* state, the $3s \rightarrow 3d$ transition is not dipole allowed. So we expect its cross section to be more sensitive than $\sigma_{3s \rightarrow 3p}$ to high-lying target states in the close-coupling representation of the target. As shown in Fig. 5, states above 3*d* (the highest in a 4CC calculation), are indeed important at energies from the 3*d* threshold to several eV above it. The cross section for $3s \rightarrow 4s$ is of comparable magnitude to $\sigma_{3s \rightarrow 3d}$ and, as seen in Fig. 6, exhibits a similar sensitivity to high-lying target states. As expected, 7CC calculations reproduce the magnitude and large-scale shape but not the detailed features in this cross section. The 10CC calculations do, however, produce these features, and comparison to 11CC results show them to be well converged even in these details.

Phelps and Lin [14] have measured both of these cross sections, and in Figs. 5 and 6 we compare our theoretical results to their data, as corrected for cascade contributions and polarization anisotropy. For the $3s \rightarrow 3d$ excitation the most important cascade corrections come from excited *f* states, the transition probabilities for $np \rightarrow 3d$ $(n > 3)$ being quite small. Since cascades contribute at most 20% of the population of the 3*d* state, Phelps and Lin place a 15% precision estimate on their cross sections; their estimate was the basis for the error bars in

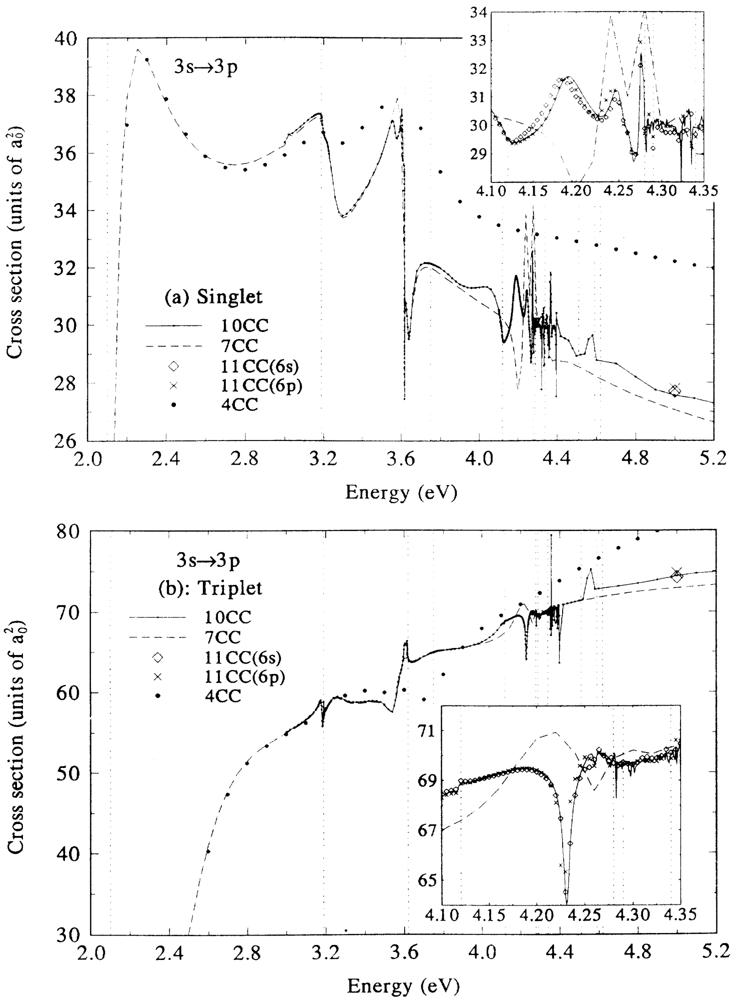

FIG. 4. Convergence of weighted (a) singlet and (b) triplet e-Na integrated $3s \rightarrow 3p$ cross sections from coupled-channel R-matrix calculations of Table II: 11CC with 6s (open diamonds), 11CC with 6p (crosses), 10CC (solid curve), 7CC (dashed curve), and 4CC (closed circles). The small dots on the 10CC curves show the energies at which these R-matrix calculations were performed. The inset details convergence of the 10CC results in the threshold-rich energy region from 4.10 to 4.35 eV.

this figure. The full width at half maximum of their electron beam, $<0.75$ eV, may explain the presence in their data listing of a point at 3.5 eV, below the 3.62-eV threshold for this excitation.

Cascade effects are much more dramatic for the $3s \rightarrow 4s$ cross section. To generate this cross section from their measured optical excitation function, Phelps and Lin use a linear model that automatically allows for multistep cascades. They first divide $Q_{4s,3s}$ by the branching ratio to produce an *apparent* cross section for the 4s level, then subtract a term that allows for cascade from higher levels:

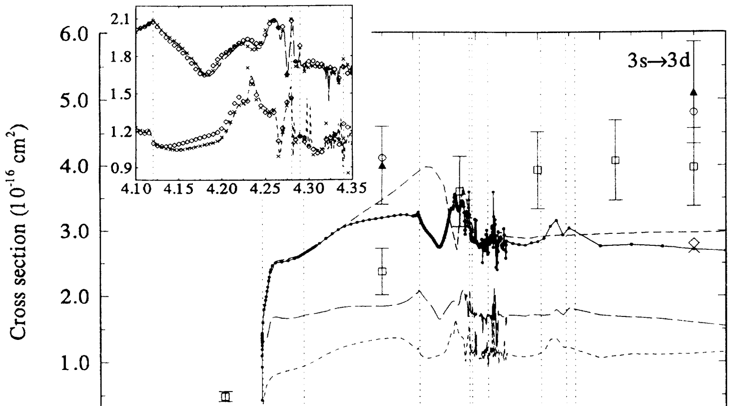

FIG. 5. Comparison of $3s \rightarrow 3d$ e-Na integrated cross sections to experimental data of Phelps and Lin (Ref. [14]) with cascade corrections (open boxes) and Stumpf and Gallagher (solid triangles) corrected as described in the text with error bars as in Ref. [15]. Theoretical results are from 11CC with 6s (open diamonds), 11CC with 6p (crosses), 10CC (solid curve), and 7CC (dashed curve) R-matrix calculations as in Table II. Also shown are the singlet (long-dashed curve) and triplet (short-dashed curve) components of the 10CC results, and the 4CC results of Moores and Norcross (Ref. [1]) (open circles).

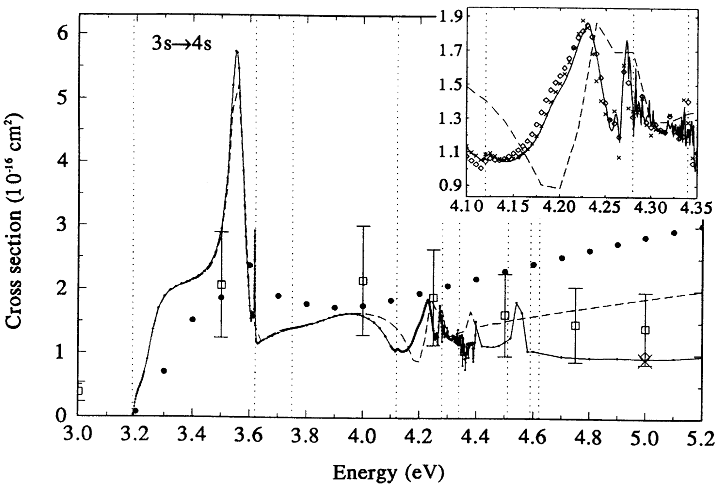

FIG. 6. Comparison of $3s\rightarrow4s$ $e$-Na integrated cross sections to experimental data of Phelps and Lin (Ref. [14]) with cascade corrections (open boxes). Theoretical results are from 11CC with $6s$ (open diamonds), 11CC with $6p$ (crosses), 10CC (solid curve), 7CC (dashed curve), and 4CC (closed circles) $R$-matrix calculations as in Table II.

$$\sigma_{3s\rightarrow4s}=\frac{1}{A_{4s,3s}\tau_{3s}}Q_{4s,3s}-\sum_{nl>4s}\frac{A_{nl,nl}}{A_{n'l',nl}}Q_{n'l',nl}\,, \qquad (4.2)$$

where $A_{nl,n'l'}$ is the spontaneous radiation probability for the $nl\rightarrow n'l'$ transition (the Einstein $A$ coefficient), and $\tau_{nl}$ is the radiative lifetime of the $nl$ level (so $A_{4s,3s}\tau_{3s}$ is the aforementioned branching ratio). The excitation function $Q_{nl,n'l'}$ in the second term corresponds to an *experimentally observable* transition originating in a state $nl$ that cascades to the $4s$ state. Writing the cascade correction in this form allows for the possibility that $Q_{nl,4s}$ may be unobservable. Of the cascade contribution to $\sigma_{3s\rightarrow4s}$, 85% comes from the $4p$ state. Consequently this cross section is strongly dependent on the transition probabilities in Eq. (4.2) for $4p\rightarrow4s$ and $4p\rightarrow3s$. Uncertainties in these quantities led Phelps and Lin to estimate the precision of this cross section at 40%.

Noting that the 4CC $3s\rightarrow3d$ cross sections of Moores and Norcross are significantly higher than their experimental results, Phelps and Lin suggest that this difference may be due to an incomplete representation of the continuum in the theoretical calculations. But Fig. 5 and Fig. 6 show that, as for $\sigma_{3s\rightarrow3p}$, improved inclusion of higher-lying states actually exacerbates the disagreement between theory and experiment. Not unexpectedly, the theoretical results in these figures further show that in the region of rich structure between 4.0 and 4.5 eV, where the thresholds for $5s$, $4d$, $4f$, and $5p$ occur, both $\sigma_{3s\rightarrow3d}$ and $\sigma_{3s\rightarrow4s}$ are acutely sensitive to the representation of the target.

The only other experimental investigation of the $3s\rightarrow3d$ excitation appears in a study by Stumpf and Gallagher [15], the primary focus of which is electron scattering from excited Na atoms. In their crossed-beam experiments a large fraction of the target atoms are first optically excited to the desired excited level (resulting in a nonstatistical mixture of magnetic sublevels), then a beam of electrons excites these atoms to higher-lying states. Stumpf and Gallagher measure the intensity of the subsequent $3d$ fluorescence as a function of electron energy and normalize the resulting excitation functions to first Born cross sections at 200–1000 eV. For the $3s\rightarrow3d$ excitation they report only the (normalized) apparent optical excitation function with an estimated uncertainty of 15%. We have corrected these data for cascade and anisotropy effects using Table II of their paper, and in Fig. 5 compare the corrected results (with the original error bars quoted by Stumpf and Gallagher) to our calculated cross sections.

Stumpf and Gallagher note an exceptionally rapid onset of $\sigma_{3s\rightarrow3d}$ at threshold, where this cross section rises to about 75% of its maximum value within 0.1 eV. This behavior is evident in both the singlet and triplet theoretical cross sections in Fig. 5 and, as shown in Fig. 7, contrasts strikingly with the threshold onset of $\sigma_{3s\rightarrow4p}$. The complexity and richness of these and other threshold structures precludes their consideration at length here; they will be the topic of a forthcoming paper [105].

### 3. *Excitation of the 4p state*

We conclude this study of integral excitation cross sections with the $3s\rightarrow4p$ cross section. In their determination of excitation functions and integrated cross sections (corrected for cascade and anisotropy effects) for this excitation, Phelps and Lin [14] note that cascade effects contribute about as much as does direct excitation, with $s$ and $d$ high-lying excited states of roughly equal importance. Because of uncertainties in corrections for these effects, they place the precision of their experimental $\sigma_{3s\rightarrow4p}$ at 40%.

In a more recent study, Marinković, Wang, and Gallagher [16] measured optical excitation functions for several highly excited states of Na near their respective thresholds. We show their results for the $3s\rightarrow4p$ excitation along with those of Phelps and Lin in Fig. 8. Since Marinković, Wang, and Gallagher normalized their data to the "apparent" excitation cross sections of Phelps and Lin [14], these data do not include cascade corrections. (It has, however, been corrected for the anisotropy of the fluorescence polarization.) Comparison to their experimental results, therefore, is least ambiguous below 4.12 eV, the threshold for excitation of the next-highest excited state, $5s$, (indicated by the small arrow in Fig. 8).

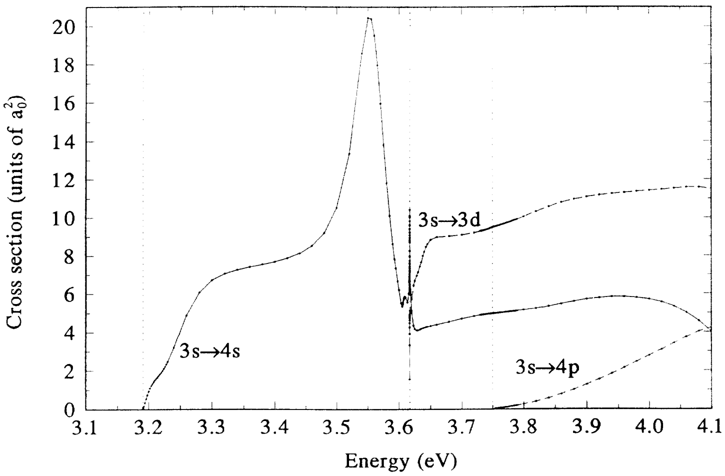

FIG. 7. Near-threshold integrated *e*-Na cross sections for the $3s \rightarrow 4s$ (solid curve), $3s \rightarrow 3d$ (long-dashed curve), and $3s \rightarrow 4p$ (short-dashed curve) excitations.

Marinković, Wang, and Gallagher remarked upon a distinct difference between the near-threshold behavior of their measured excitation functions for *p* states and those for *s* and *d* states; the theoretical near-threshold results in Fig. 7 confirm the origin of this difference in the relevant cross sections.

### *4. The total and elastic cross sections*

Finally we turn to the total cross section $\sigma_{\text{tot}}$ defined in Eq. (4.1). As we saw in Fig. 2, just above the first excitation threshold the elastic $3s \rightarrow 3s$ component dominates this cross section. By breaking the elastic cross section into contributions from the singlet and triplet spin channels in Fig. 9 we find that $\sigma_{3s \rightarrow 3s}$, in turn, is overwhelmingly dominated by triplet scattering. This figure also shows a convergence study for this important cross section. Near the thresholds for various excitations, intricate structures appear in $\sigma_{3s \rightarrow 3s}$ in both singlet and triplet channels: a structure near the 5*s* threshold at 4.12 eV, for example, is evident in the singlet channel, while one near the 3*d* threshold at 3.62 eV exhibits effects in both spin channels. As we have seen in inelastic cross sections, such structures emerge only when high-lying $n \geq 4$ states are included in the target-state expansion. Figure 9(a) shows, moreover, that details of the triplet structure near the 5*s* threshold are extremely sensitive to the $n=5$ states in the 10CC and 11CC calculations. At higher energies, the elastic cross section settles down, and calculations including $n=5$ and 6 states show that these states are no longer necessary; the 7CC are quite well converged.

Kasdan, Miller, and Bederson [12] have measured the total cross section in atom-beam recoil experiments. Their experiments differ radically from those discussed so far: in them, the fundamental observed quantity is the attenuation due to electron scattering of the intensity of the atomic beam in the forward direction. From this quantity Kasdan, Miller, and Bederson determine *absolute* cross sections within an estimated statistical and systematic uncertainty of 13% below 4 eV and 12% above. We compare our and their results in Fig. 10, where we see that except at and above 4.0 eV the agreement between experiment and theory is excellent. Also shown in this figure is a single data point from the recent measurements of Kwan *et al.* [17], an extensive study using a beam-transmission technique of electron and positron scatter-

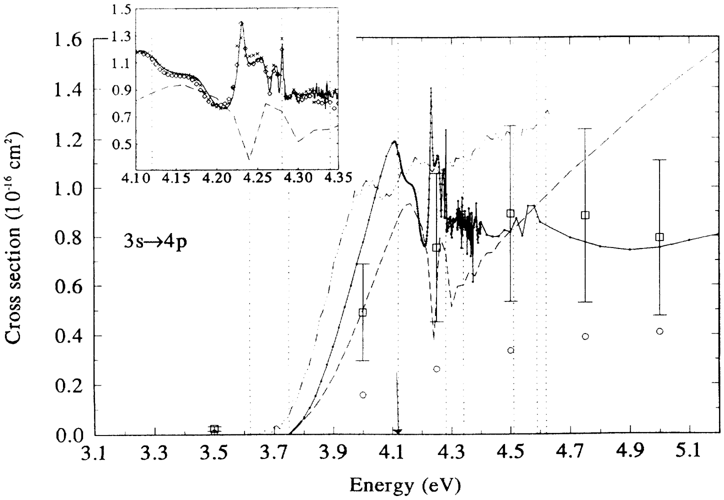

FIG. 8. Comparison of $3s \rightarrow 4p$ *e*-Na integrated cross sections to experimental data of Marinković, Wang, and Gallagher (Ref. [16]) (dot-dashed curve) and Phelps and Lin (Ref. [14]), the latter with (open circles) and without (open boxes) cascade corrections. Theoretical results are from 10CC (solid curve) and 7CC (dashed curve) *R*-matrix calculations as in Table II. Thresholds are shown as in Fig. 2. The inset shows results from 11CC with 6*s* (open diamonds) and 11CC with 6*p* (crosses) calculations to demonstrate convergence at energies from 4.10 to 4.35 eV.

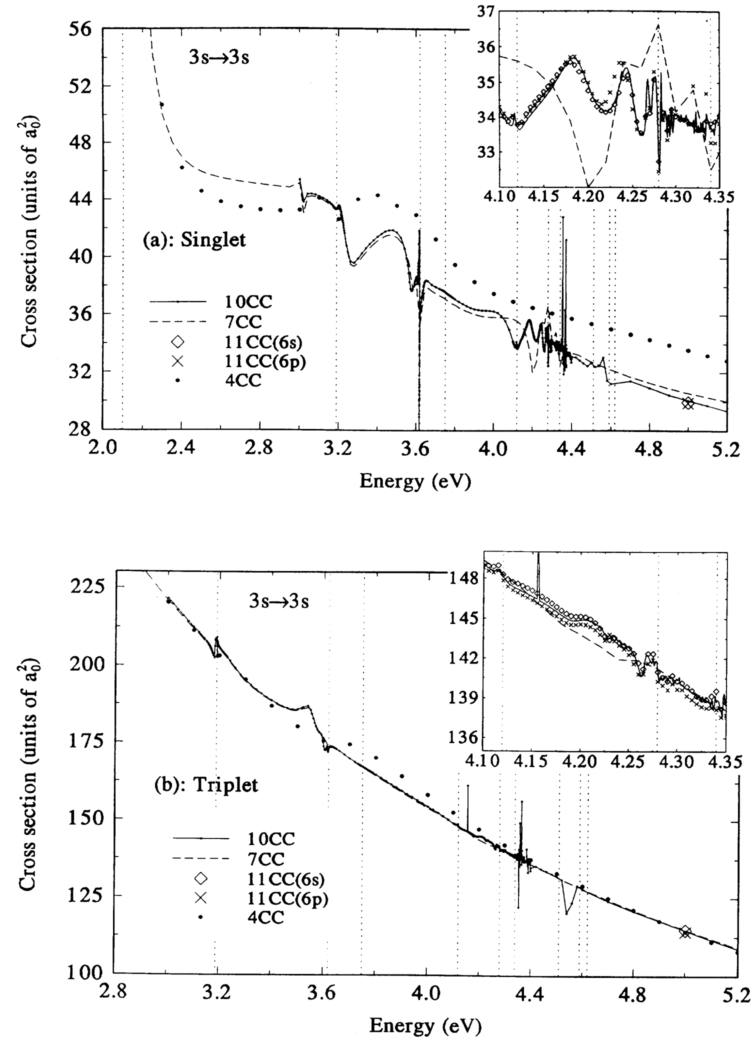

FIG. 9. Convergence of weighted (a) singlet and (b) triplet *e*-Na integrated elastic cross sections from coupled-channel *R*-matrix calculations of Table II: 11CC with 6*s* (open diamonds), 11CC with 6*p* (crosses), 10CC (solid curve), 7CC (dashed curve), and 4CC (closed circles). The small dots on the 10CC curves show the energies at which these *R*-matrix calculations were performed. The inset shows additional 11CC results to demonstrate convergence of the 10CC cross sections at energies from 4.10 to 4.35 eV.

ing from Na at energies up to 102 eV. To clarify the role of elastic scattering in the energy range of these experiments and the origin of the structures in $\sigma_{\text{tot}}$, we also show the elastic and largest inelastic cross sections $\sigma_{3s\to 3p}$.

To conclude, we compare integrated elastic and inelastic ($3s \to 3p$) cross sections to the results of another highly accurate but quite different theoretical calculation. We are fortunate to have available *e*-Na scattering amplitudes from the nonrelativistic coupled-channel optical-potential (CCO) [106–112] calculations that Bray has performed at 1.0, 1.6, and 4.1 eV [106,107,111,112]. This method has been reviewed by McCarthy [108], its formal background surveyed by McCarthy and Weigold [109], and its application to *e*-Na scattering reviewed by Bray [110]. Like the present approach, the CCO method is based on an expansion in a finite set of target states within the independent particle model using a frozen Hartree-Fock $\text{Na}^+$ core, and includes the nonlocal exchange potential exactly. Unlike the present approach, it entails numerical solution of the integral partial-wave

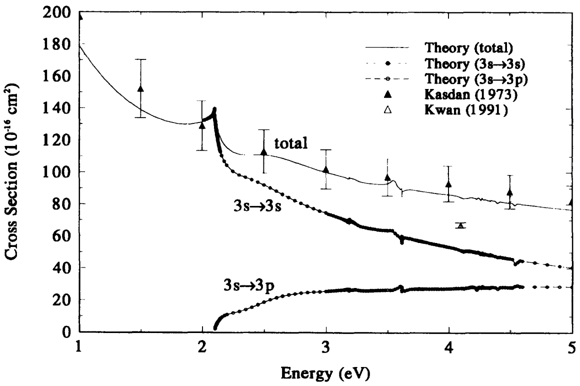

FIG. 10. Comparison of theoretical (10CC) integrated total *e*-Na cross section to experimental results of Kasdan, Miller, and Bederson (Ref. [12]) (closed triangles) and Kwan *et al.* (Ref. [17]) (open triangles). To show the contribution of the dominant cross sections to this quantity [see Eq. (4.1)] we also include the elastic (long-dashed curve) and $3s \to 3p$ (medium-dashed curve) cross sections.

scattering equations in momentum space (the Lippmann-Schwinger equation for the $T$ matrix) [113] in which high-lying target states (and the ionization continuum) are represented via a complex, nonlocal, energy-dependent polarization that, together with the static and exchange potentials, constitute the eponymous optical potential [111]. The central approximation of the CCO method is modeling the amplitudes for excitation of the states included in the polarization potential making approximation that the coupling of these states is weak.

In Table IV we compare $R$-matrix, 15CC, and CCO integrated cross sections at 1.0, 1.6, and 4.1 eV. Two points are worthy of comment. First, although the methods use completely different numerical strategies to solve the Schrödinger equation the agreement is good. Second, both the model polarization potential we have implemented, Eqs. (3.1)–(3.4) and the optical potential of the CCO method, appear to be comparably accurate representations of this aspect of the physics of $e$-Na scattering. The CCO method, however, does not allow for dielectronic polarization, which we include via the model defined in Eq. (3.4). As Table IV shows, although at these energies dielectronic polarization effects are not enormous, their omission does alter these cross sections to within the accuracy of the present calculations—changing, for example, the singlet integrated cross sections at these energies by as much as 6%. We shall return to comparison to CCO results in Sec. IV B on differential cross sections.

TABLE IV. Comparison of integrated elastic and $3s \rightarrow 3p$ cross sections (in square bohr) from 10CC $R$-matrix and coupled-channel optical-potential (Ref. [106]) calculations. To demonstrate convergence of the 10CC results, we also show $R$-matrix cross sections for 4CC at 1.0 and 1.6 eV, and for 7CC at 4.1 eV. Also shown are 10CC $R$-matrix cross sections calculated *without* inclusion of the dielectronic polarization potential of Eq. (3.4).

| | $3s \rightarrow 3s$ | | |
|---|---|---|---|
| | Singlet | Triplet | Total |
| 1.0 eV | | | |
| 10CC | 77.569 | 561.69 | 639.26 |
| 4CC | 77.50 | 560.43 | 637.93 |
| 10CC (no dielectronic) | 81.699 | 564.45 | 646.15 |
| 15CC (Bray, Ref. [106]) | 84.00 | 563.00 | 647.00 |
| 1.6 eV | | | |
| 10CC | 92.669 | 391.07 | 483.74 |
| 4CC | 92.48 | 389.45 | 481.93 |
| 10CC (no dielectronic) | 98.685 | 397.33 | 496.02 |
| 15CC (Bray Ref. [106]) | 103.2 | 399.1 | 502.3 |
| 4.1 eV | | | |
| 10CC | 34.184 | 149.06 | 183.24 |
| 7CC | 35.742 | 149.35 | 185.09 |
| 10CC (no dielectronic) | 35.717 | 153.72 | 189.44 |
| CCO | 37.26 | 159.14 | 196.4 |
| | $3s \rightarrow 3p$ | | |
| 4.1 eV | | | |
| 10CC | 30.053 | 68.330 | 98.859 |
| 7CC | 30.34 | 67.01 | 97.35 |
| 10CC (no dielectronic) | 30.880 | 70.322 | 101.12 |
| CCO | 30.34 | 67.01 | 97.35 |

### B. Differential cross sections

Because differential cross sections (DCS's) are more sensitive than integrated cross sections to details of the scattering matrix, they afford an excellent medium for comparing theoretical and experimental results. For $e$-Na, the availability of measured DCS's for well-defined changes in the projections of the spin and orbital angular momenta make possible an unusually sensitive comparison of this kind, as we shall see in the next subsection. Here we consider elastic and inelastic ($3s \rightarrow 3p$) DCS's, paying special attention to the much-studied cusp in $\sigma_{3s \rightarrow 3s}$ near the $3p$ threshold at $\epsilon_{3p} = 2.10$ eV.

### *1. Elastic $3s \rightarrow 3s$ DCS*

Elastic scattering occurs predominantly in the forward direction, and this DCS is comparatively structureless. Structures do appear, however, for fixed scattering angles as a function of energy near excited-state thresholds: e.g., near 3.62 ($\epsilon_{3s}$) and 4.2 eV (in the vicinity of $\epsilon_{5s} = 4.12$ eV, $\epsilon_{4d} = 4.28$ eV, and $\epsilon_{4f} = 4.29$ eV). The most pronounced (and most thoroughly investigated) near-threshold structure occurs near the $3p$ threshold at 2.10 eV. This feature is both most pronounced and most studied for the same reason: near this threshold, strong coupling of the elastic and $3s \rightarrow 3p$ channels enhances the effect of the $(E_0 - \epsilon_{3p})^{1/2}$ factor that governs the shape of the elastic DCS very near this threshold [79,114–118].

Before discussing experimental measurements of the elastic DCS, we compare our converged results to those of the CCO calculations of Bray, Konovalov, and McCarthy [111] (see Sec. IV A) 1.0, 1.6, and 4.1 eV in Fig. 11. The excellent agreement between these two quite different theoretical calculations of this sensitive scattering quantity supports the validity of the two quite different representations of the polarization interaction used in these studies, and suggests that at these energies the effect of the full optical potential used by Bray, Kono-

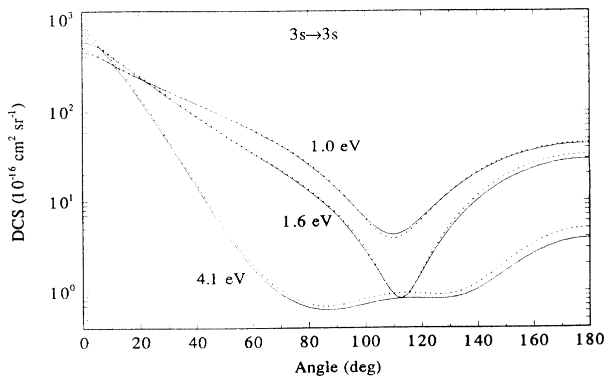

FIG. 11. Theoretical elastic DCS from 10CC $R$-matrix (solid curves) and CCO (dotted curves) calculations of Bray (Ref. [106]) at 1.0, 1.6, and 4.1 eV (Ref. [112]).

valov, and McCarthy is small.

Andrick, Eyb, and Hofmann [7] and Eyb and Hofmann [9] first reported observations of the cusp at $\epsilon_{3p}$ in crossed-beam measurements of relative elastic cross sections normalized (at 1.6 eV) to the 4CC theoretical results of Moores and Norcross [1]. These authors emphasize that the importance of cusp features is not due solely to their considerable theoretical interest: "[*a*]*s* the edges and cusps are so well defined they are assumed to lie at threshold and as the threshold energy is known exactly the cusps are a powerful means for energy calibration." Perhaps in consequence this feature has also been studied in experiments by Gehenn and Reichert [6] and (at 90° only) by Hafner [8].

To see the origin of this structure, we show in Fig. 12(a) the singlet and triplet *partial* elastic cross sections for *s*, *p*, and *d* waves [as defined in Eq. (3.29) with $\gamma=\gamma_0$]. Clearly, the near-threshold cusp arises from the *singlet p-wave* contribution to the elastic cross section. We also see clear indications of structure in the singlet *d*-wave cross section; Eyb and Hofmann attribute this feature to a resonance just below the 3*p* threshold. By contrast, the magnitude of the triplet scattering amplitude, although larger than the singlet and hence an important determinant of the magnitude of the elastic cross section, does not contribute to its distinctive behavior near $\epsilon_{3p}$.

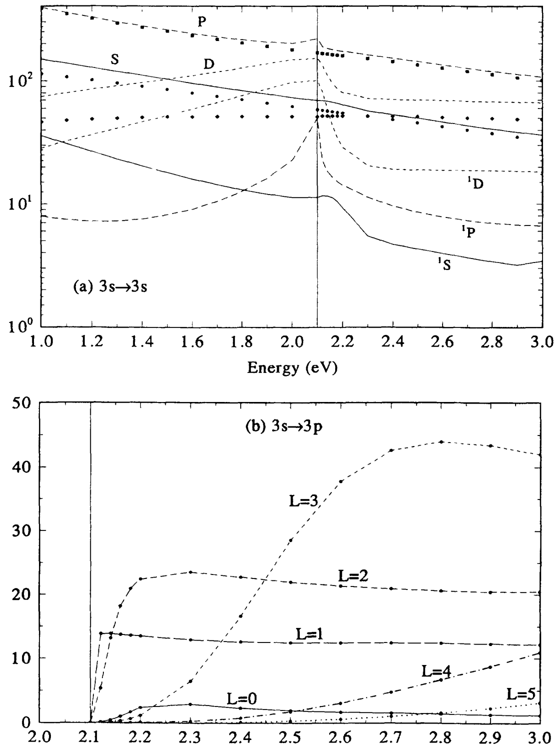

FIG. 12. Partial-wave contributions to the (a) elastic and (b) inelastic $3s\rightarrow3p$ *e*-Na cross section near the 3*p* excitation threshold. These partial cross sections, which are defined by Eq. (3.29), are labeled by total orbital and spin angular momentum quantum numbers $\mathcal{L}$ and spin $\mathcal{S}$, respectively. In (a) we show singlet, triplet, and total elastic cross sections for *S* (solid curves), *P* (medium-dashed curves) and *D* (short-dashed curves) waves. In each case the singlet and total cross sections are denoted by (labeled) lines and the triplet cross sections by symbols, as *S* (closed circles), *P* (closed boxes), and *D* (closed triangles). In (b) we show the near-threshold behavior of the first six inelastic partial-wave contributions, including both singlet and triplet terms, with each curve labeled by its partial-wave order.

The particular character of the cusp arises from the interaction near $\epsilon_{3p}$ of the 3*s* and 3*p* channels. To clarify this interaction, we show in Fig. 12(b) the partial *inelastic* cross sections for the $3s\rightarrow3p$ excitation. The inelastic *p* wave clearly exhibits the behavior of a nearly bound state. Moreover, the rapid rise of the inelastic *d*-wave cross section explains the precipitous drop in its elastic counterpart in Fig. (12a).

The dramatic effect of these near-threshold features on the elastic DCS is evident in the three-dimensional overview of Fig. 13, and in the more detailed two-dimensional comparisons in Fig. 14. The first figure shows fairly well-defined regions of energy and angle where the cusp effect is most pronounced. The breakdown of this cross section into singlet and triplet DCS's at selected near-threshold energies in Fig. 14 emphasizes the importance of the triplet contribution. Although the singlet cross section causes structure in the elastic DCS, the triplet spin channel is primarily responsible for its overall shape. But this DCS emphasizes forward scattering; so the cusp we saw in the *integrated* cross section in Fig. 3 is almost entirely due to variations in the *singlet* contribution at angles below about 40°.

The near-threshold structure in the singlet DCS is considerably more dramatic below than above $\epsilon_{3p}$: this cross section changes a great deal between 1.0 and 1.5 eV but very little between 2.5 and 3.0 eV. It clearly does not manifest the behavior one would expect were the singlet-*p* cusp in control: in that case the resulting $P_1(\cos\theta)$ dependence would force the DCS to zero at 90°. Instead, the singlet-*d* resonance, which becomes important away from threshold, ultimately overpowers the singlet-*p* cusp, giving the DCS an overall shape characteristic of almost

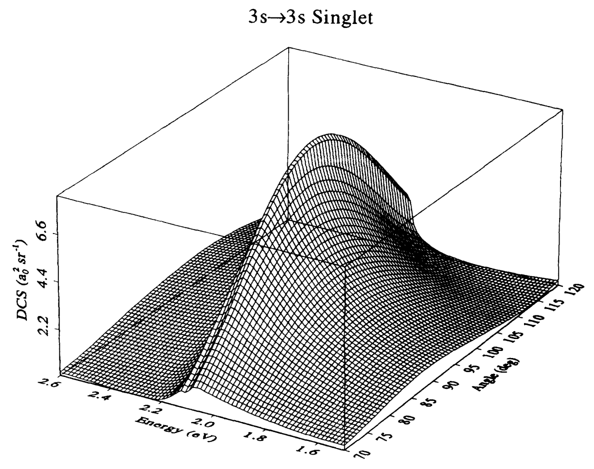

FIG. 13. Overview of the angular and energy dependences of the elastic differential *e*-Na cross section near the 3*p* threshold at 2.10 eV.

pure *d*-wave scattering. Moreover, the $(E_0-\epsilon_{3p})^{3/2}$ energy dependence introduced by this resonance broadens the cusp.

In Fig. 15 we show theoretical (7CC) elastic DCS's *as functions of energy at selected fixed scattering angles,* compared to the relative angular distributions of Eyb and Hofmann, which, following their recommended prescription, we have renormalized at each angle at 1.6 eV. Converging these DCS's at this energy is rather easy; as the comparisons in these figures demonstrate, four states is quite sufficient. Although some differences with the measured data are apparent (e.g., at 20°), theory and experiment agree throughout the measured angular range from 20° to 145° on the general features of the DCS: the dramatic diminution of the cusp near 60°, its striking reappearance near 90°, and its persistence to about 120°. The disappearance of the cusp near 60°, which Eyb and Hofmann remark as "unexplained," is here revealed to be a consequence of the dominance of triplet scattering in this angular range. The triplet DCS at angles near 60°, shown as a function of energy in Fig. 14(b), does not exhibit any structure; neither do the observed angular distributions. Gehenn and Reichert [6] and Ying *et al.* [119] and Vušković [120] have also measured this DCS at 2.1 eV, and in Fig. 16 we compare their data to our cross sections. Particularly notable is how well the relative angular distributions from the early measurements by Gehenn and Reichert show the distinctive shape of this DCS over essentially the whole angular range. Theirs is the only experiment to date to report relative DCS's at energies above 2.0 eV, and in Fig. 17 we show their and our results at 5.0 and 8.0 eV along with detailed convergence studies at these energies. The quality of convergence and agreement with this experiment at these higher energies is comparable to that seen at 2.1 eV in Fig. 16.

Although the cusp near 2.10 eV has received the lion's share of experimental attention, data are available at a few other energies. The most recent such study is the recoil atom experiment of Ying *et al.* [119]. From the ratio of the measured intensities of unscattered Na atoms and those recoiling from the collision with electrons in a beam, these authors determine absolute DCS's at energies from 0.5 to 3.0 eV for angles from 1° to 60°. In Fig. 18 we show representative comparisons of our results to theirs and to the relative angular distributions of Gehenn and Reichert [6] (normalized to our DCS at 60°). The quality of the agreement here and at the other energies studied (except 0.5 eV) is very good. Comparison to the 7CC results at 3.0 eV show that at these energies four states are quite adequate for this cross section. By 4.0 eV, as shown in Fig. 18(b), the $n=4, l>0$ states included in the 7CC calculations (and less so the $n>4$ states in the 10CC calculations) begin to (minimally) affect the shape of the elastic DCS.

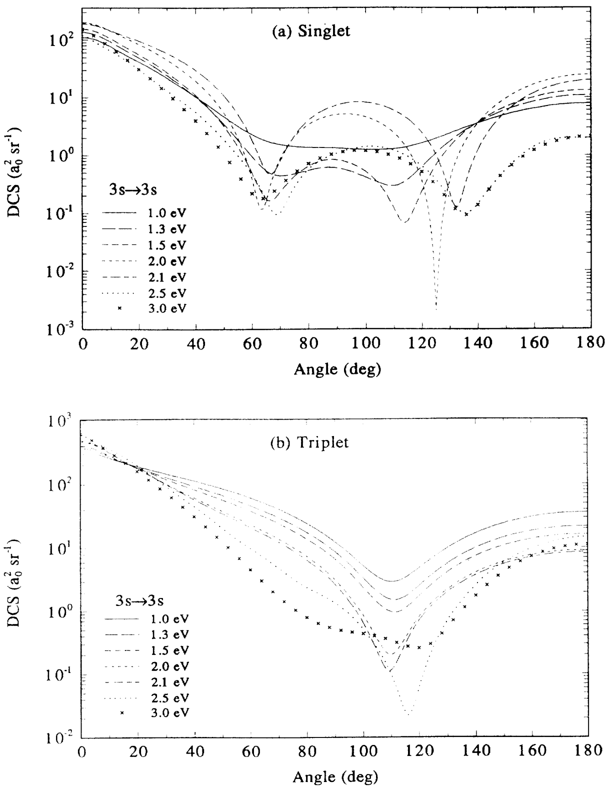

FIG. 14. Behavior of weighted (a) singlet and (b) triplet elastic differential cross sections at selected energies near the 3*p* threshold: 1.0 (solid line), 1.3 (long-dashed line), 1.5 (medium-dashed line), 2.0 (short-dashed line), 2.1 (alternating dashed line), 2.5 (dots), and 3.0 eV (crosses).

### C. Inelastic $3s\to3p$ DCS

Ying *et al.* [119] have reported absolute inelastic DCS's based on data taken in atom recoil experiments at energies including 2.6, 3.0, and 3.7 eV. Their measurements at the lowest energy affords an opportunity to compare this DCS with results from the quite different crossed-beam experiments of Han, Schinn, and Gallagher [117] (see Sec. IV D). In Fig. 19(a) we see that theory and these experiments agree about the predominantly forward character of this DCS but not about its qualitative shape at intermediate and large angles. At this energy and at 3.0 eV, the level of agreement between experiment and theory is comparable to that at 2.6 eV seen in Fig. 19(a). The convergence data in Fig. 19(a) show that, as expected from convergence near the cusp at 2.10 eV, near and just above the 3*p* threshold one need include only the lowest four target states to converge elastic and inelastic cross sections. But by 3.7 eV this representation of the target is no longer adequate. As shown in Fig. 19(b), by this energy one must include $n=4$, $l>0$ Na states to generate the correct shape of this DCS. Perhaps surprisingly, even as high as 4.1 eV, the energy of Fig. 19(c), the $n>5$ states we include in our 10CC and 11CC calculations are not required for this particularly strong transition. Finally, we include in this figure the CCO inelastic DCS's of Bray [106], which, encouragingly, agree as well with ours as did the elastic DCS in Fig. 11.

Examination of inelastic and (as seen in Sec. IV B), elastic DCS's at the particular energies where measurements have been made may not reveal the full richness of their behavior, especially near thresholds for higher excitations. So we close by surveying, in the three-dimensional plots of Fig. 20, the differential cross sections for $3s \rightarrow 3p$ and $3s \rightarrow 4s$. The two are strikingly different in character. With increasing energy, forward scattering comes to dominate the (dipole allowed) $3s \rightarrow 3p$ cross section, while the (dipole forbidden) $3s \rightarrow 4s$ exhibits a variety of complicated structures in both forward and backward directions. Experimental measurements of these subtly varying angular distributions would provide an invaluable aid to assessing the assumptions underlying the present and other theories.

### D. Spin- and orbital-angular-momentum-changing cross sections

In a series of remarkable experiments Han, Schinn, and Gallagher [116,117] determined integral [116] and differential [117] $3s \rightarrow 3p$ cross sections corresponding to well-defined changes in the projections of the spin ($|\Delta M_S| = M_S' - M_S$) and/or orbital ($|\Delta M_L| = M_L' - M_L$) angular momentum of the valence Na electron (where primes denote the final state). These data approach a complete description of the collision [50] in terms of con-

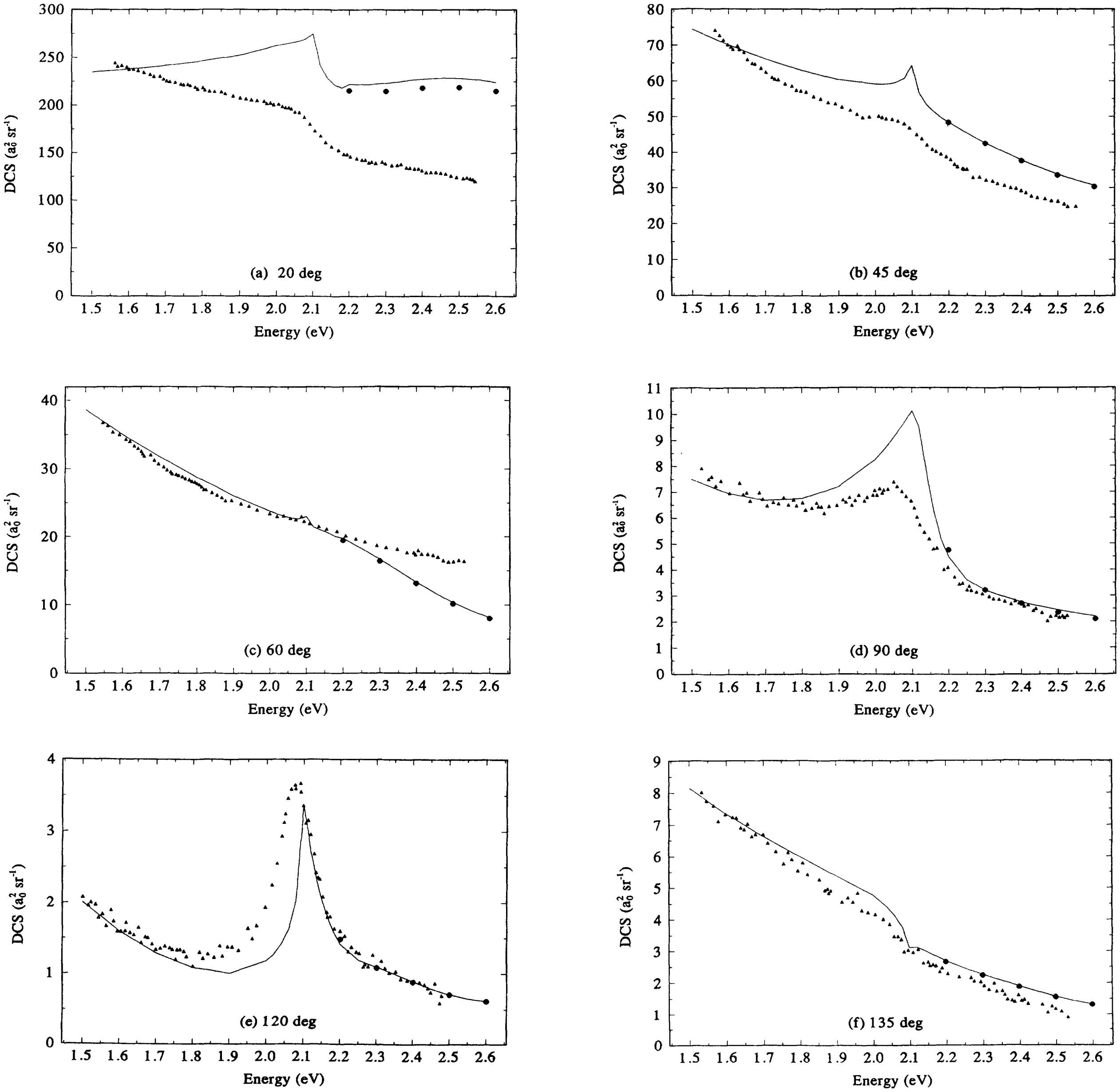

FIG. 15. Comparison of theoretical elastic $e$-Na differential cross sections as functions of energy at selected angles to the experimental results of Eyb and Hofmann (Ref. [9]) (closed triangles): (a) 20°, (b) 45°, (c) 60°, (d) 90°, (e) 120°, and (f) 135°. In each case, the theoretical data are from 7CC (solid curves) and 4CC (closed circles) calculations, to which the data of Eyb and Hofmann at 1.6 eV has been normalized.

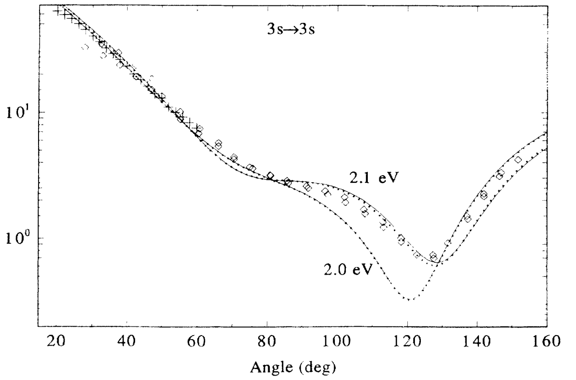

FIG. 16. Theoretical elastic differential cross sections at 2.0 and 2.1 eV compared to absolute experimental data from Vušković (Ref. [120]) (pluses) (at 2.0 eV) and Gehenn and Reichert (Ref. [6]) (open diamonds) (at 2.1 eV). To illustrate convergence of the 4CC results (dotted curves) at this energy, we also show 7CC DCS (solid curves) cross sections.

ventional scattering quantities (as opposed to orientation and alignment parameters); in particular, the four independent cross sections $\sigma^{|\Delta M_S|}_{|\Delta M_L|}(\theta)$ (see below) can be regarded as four of the seven independent quantities needed to fully describe the $3s \longrightarrow 3p$ excitation. These cross sections also permit a more sensitive probe of theoretical models and approximations than do the usual inelastic differential (or worse, integrated) cross sections—which amount to sums of the quantities measured by Han, Schinn, and Gallagher. In effect, these experiments probe features of the scattering matrix that are masked in more traditional cross sections. They have clarified, among other things, the importance of exchange effects in the $3s \longrightarrow 3p$ transition—effects whose investigation otherwise would require knowledge of the spin polarization of the electrons, atoms, or both.

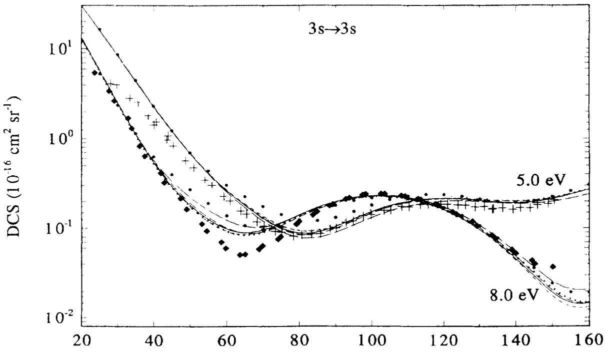

FIG. 17. Elastic differential *e*-Na cross sections from various *n*CC theoretical calculations compared to relative angular distributions measured by Gehenn and Reichert (Ref. [6]) at 5.0 (solid diamonds) and 8.0 eV (pluses). The theoretical results are from the following calculations: 4CC (closed circles), 7CC (long-dashed curve), 9CC (medium-dashed curve), 10CC (solid curve), 11CC with 6*s* (dotted curve), and 11CC with 6*p* (short-dashed curve). The basis sets used in these calculations are described in Table II.

An earlier theoretical paper [55] compared *R*-matrix results to experimental *integrated* angular-momentum-changing cross sections; the present discussion focuses on their differential counterparts. The convergence properties of the integrated angular-momentum-changing cross sections in Fig. 21 show that one must include a full complement of ten states in order to produce some of the rich structure at high excitation thresholds in the energy range from 2.1 to 8.6 eV.

In their crossed-beam experiment, Han, Schinn, and Gallagher first use optical pumping techniques to prepare the atoms in a pure spin substate of the ground $3\,^2S$ state of Na. They then use an electron beam to excite various (Zeeman separated) $M_J$ sublevels of the $3\,^2P_J$ term, the relative populations of which they determine by detecting fluorescence from the 4*p* state to the ground state. (In this two-step process, excited 3*p* atoms are first excited to the 5*s* state by a cw laser whose frequency sweeps across all four magnetic sublevels of the $3\,^2P$ state; these then decay to the 4*p* state. Further cascade to the ground state produces the measured photons.) From these populations they determine the aforementioned cross sections (corrected for cascade at energies above the 4*s* threshold

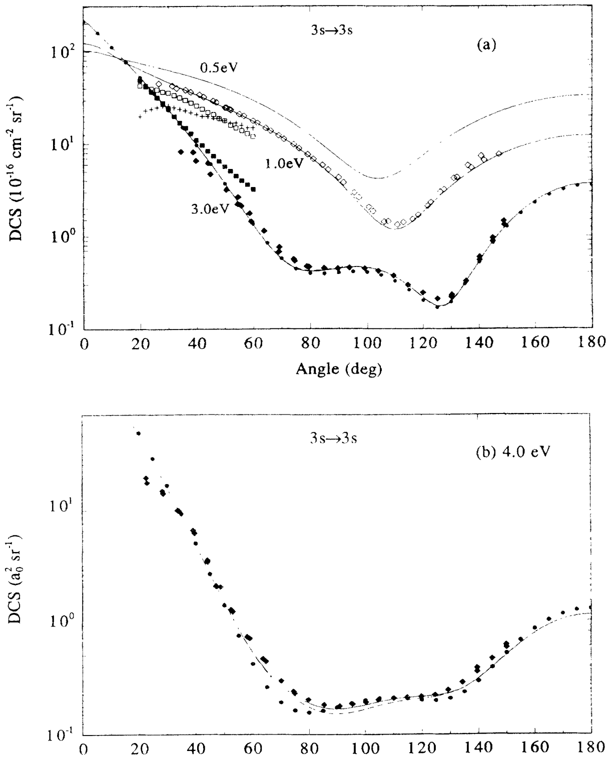

FIG. 18. Elastic *e*-Na differential cross sections from theory and experiment. Theoretical results shown are 10CC (solid curves), 7CC (dashed curves), and 4CC (closed circles). In (a), the experimental data is that of Gehenn and Reichert (Ref. [6]) at 1.0 (open diamonds) and 3.0 eV (closed diamonds), and Vušković (Ref. [120]) at 0.5 (pluses), 1.0 (open squares), and 3.0 eV (closed squares). In (b), the experimental data is that of Gehenn and Reichert at 4.0 eV (closed diamonds).

at 3.192 eV) for changes in $M_L$ and $M_S$ of the valence electron.

Because of reflection symmetry in the scattering plane defined by the incident and outgoing electron wave vectors, only four of the nine possible partial cross sections are independent; these cross sections are invariant with respect to simultaneous change of the signs of $|\Delta M_L|$ and $|\Delta M_S|$. (Since the ground state is an $s$ state, $M_L=0$; since the final state is a $P$ state, $M_L=-1,0,+1$.) This follows from the symmetry properties of the singlet and triplet scattering amplitudes ${}^{2\mathcal{S}+1}f_{3s,0\rightarrow 3p,M_L}(\theta)$ of Eq. (3.27), which we abbreviate ${}^{2\mathcal{S}+1}f_{M_L}(\theta)$:

$$ {}^{2\mathcal{S}+1}f_{-1}(\theta)=-{}^{2\mathcal{S}+1}f_{+1}(\theta) . \tag{4.3}$$

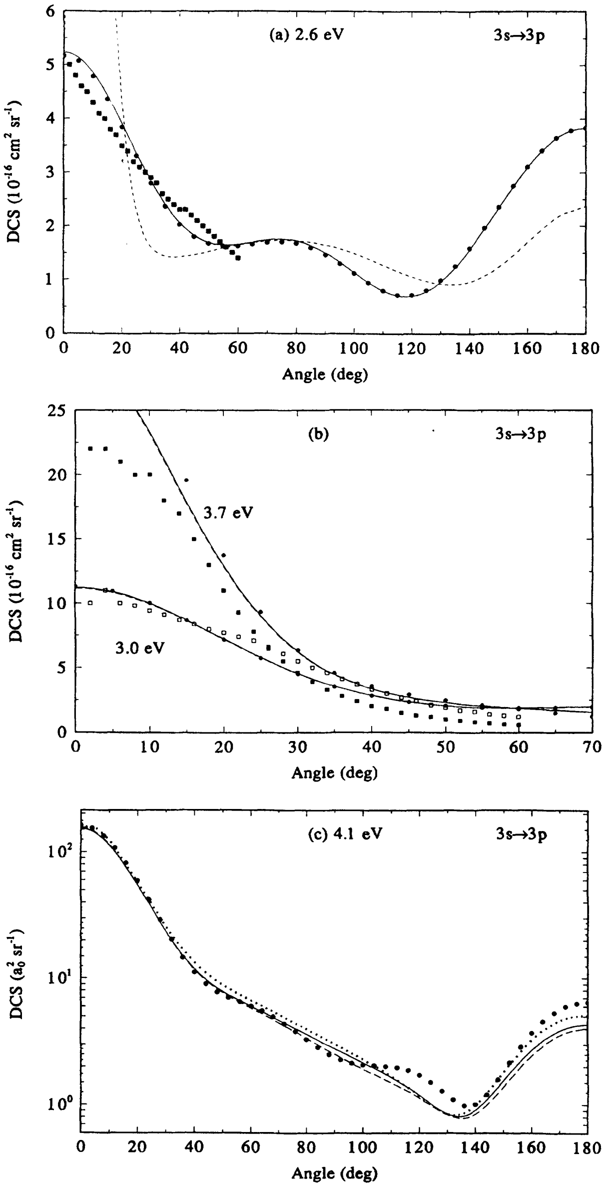

FIG. 19. Inelastic $3s\rightarrow 3p$ $e$-Na differential cross sections. (a) DCS at 2.6 eV compared to experimental results of Han, Schinn, and Gallagher (Ref. [117]) (dotted line) and of Ying *et al.* (Ref. [119]) (closed squares). (b) DCS's at 3.0 and 3.7 eV compared to the measured DCS of Ying *et al.* (labeled open and closed squares). (c) DCS at 4.1 eV compared to theoretical CCO results of Bray (Ref. [106]) (dotted curve). In each comparison, our results are cross sections from 10CC (solid curves), 7CC (dashed curves), and 4CC (closed circles) $R$-matrix calculations.

(a) 3s→3p

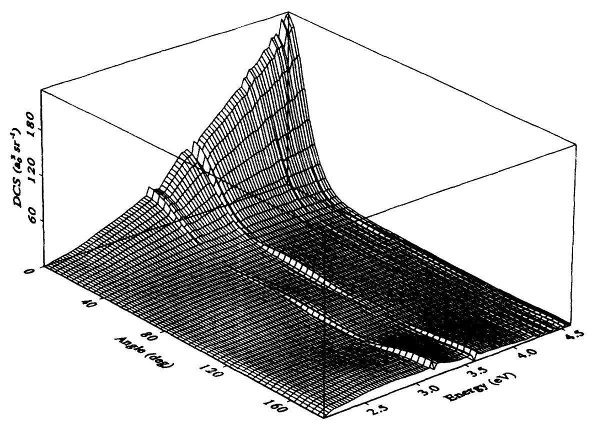

(b) 3s→4s

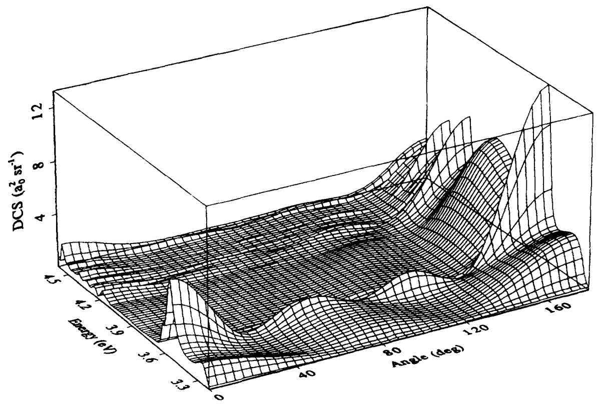

FIG. 20. Three-dimensional overview of the (a) $3s\rightarrow 3p$ and (b) $3s\rightarrow 4s$ inelastic $e$-Na differential cross sections.

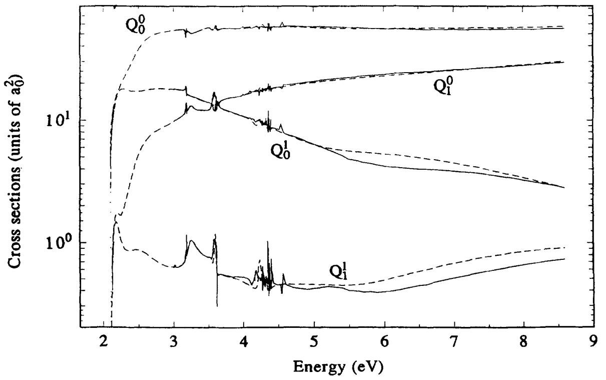

FIG. 21. Integrated angular-momentum-changing $3s\rightarrow 3p$ cross sections $\sigma_{|\Delta M_L|}^{|\Delta M_S|}(\theta)$ from 10CC (solid curves) and 7CC (dashed curves) $R$-matrix calculations.

Moreover, the weakness of the spin-orbit interaction (and the absence of other explicitly spin-dependent forces) means that these cross sections are invariant with respect to a sign change of *either* $|\Delta M_L|$ or $|\Delta M_S|$. Thus we onle consider four independent cross sections: $\sigma_1^1(\theta)$, $\sigma_0^1(\theta)$, $\sigma_1^0(\theta)$, and $\sigma_0^0(\theta)$, *where the superscript shows the change in $M_S$ and the subscript the change in $M_L$*. The *total* DCS for the $3s \to 3p$ transition is just the sum of these angular-momentum-changing cross sections; allowing for the twofold degeneracy in the case $|\Delta M_L|=1$, we have

$$\frac{d\sigma}{d\Omega}\bigg|(3s\to 3p)(\theta)=\sigma_0^0(\theta)+\sigma_0^1(\theta)+2\sigma_1^0(\theta)+2\sigma_1^1(\theta)\ . \tag{4.4}$$

In terms of the fundamental scattering amplitudes of Eq. (4.3), we can write these partial cross sections as

$$\sigma_0^0(\theta)=\frac{1}{4}\frac{k}{k_0}[\,|{}^1f_0(\theta)+{}^3f_0(\theta)|^2+2|{}^3f_0(\theta)|^2]\ , \tag{4.5a}$$

$$\sigma_0^1(\theta)=\frac{1}{4}\frac{k}{k_0}|{}^1f_0(\theta)-{}^3f_0(\theta)|^2\ , \tag{4.5b}$$

$$\sigma_1^0(\theta)=\frac{1}{4}\frac{k}{k_0}[\,|{}^1f_1(\theta)+{}^3f_1(\theta)|^2+2|{}^3f_1(\theta)|^2]\ , \tag{4.5c}$$

$$\sigma_1^1(\theta)=\frac{1}{4}\frac{k}{k_0}|{}^1f_1(\theta)-{}^3f_1(\theta)|^2\ . \tag{4.5d}$$

Han, Schinn, and Gallagher [117] report partial DCS's at 2.6, 3.1, and 3.6 eV. In comparing these results to theoretical cross sections it is important to note that the observed signal in this experiment is a convolution of the excitation cross section and the optical excitation function—itself a convolution of the natural line shape, the thermal Doppler profile, and the Doppler shift due to the atomic recoil. To extract the DCS for changes in $M_L$ and/or $M_S$ requires an extremely complex deconvolution and a least-squares fit. Han, Schinn, and Gallagher assume a fairly simple functional form for the cross section: the sum of a few Legendre polynomials, together with exponential functions to improve the fits in the forward or backward directions. One can reasonably expect such an analysis to produce cross sections of the correct overall shapes, but it is unlikely to get fine details, especially where the DCS is relatively small.

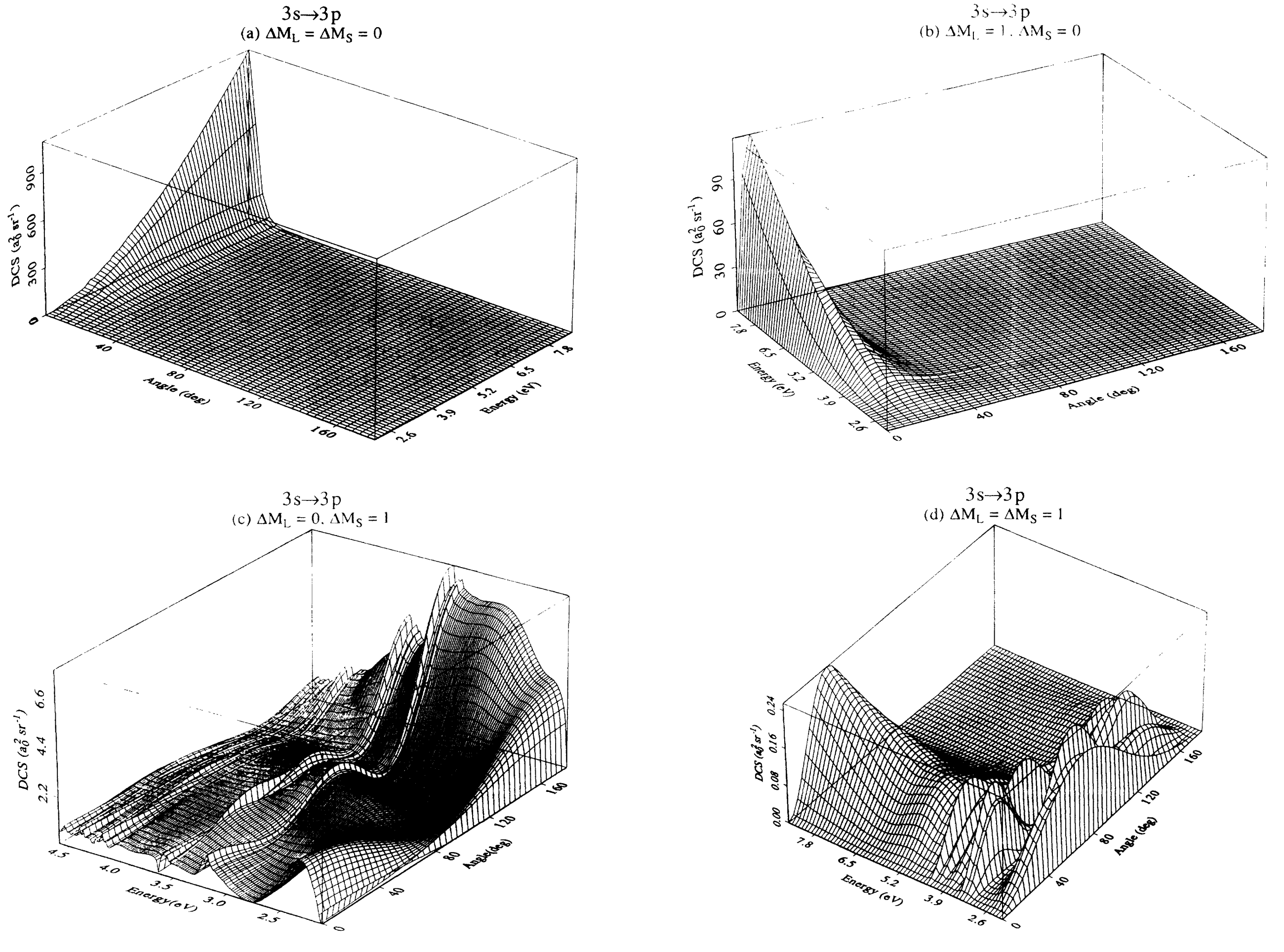

FIG. 22. Energy and angular dependence of the four independent angular-momentum-changing differential $3s \to 3p$ cross sections for $e$-Na scattering: (a) $\sigma_0^0(\theta)$, (b) $\sigma_1^0(\theta)$, (d) $\sigma_0^1(\theta)$, and (d) $\sigma_1^1(\theta)$.

To provide a context for the particular energies at which we compare to experiment, we provide in Fig. 22 a bird's-eye view of all four as functions of angle and energy. The DCS's that correspond to a change in $M_L$ and/or $M_S$ exhibit a wealth of structure, especially in the threshold-rich energy region from 2.1 to 4.6 eV. Especially splendid is the terrain in Fig. 22(d) for $\sigma_1^1(\theta)$, the smallest of the four cross sections.

The non-angular-momentum-changing cross section $\sigma_0^0(\theta)$, which dominates the total $3s\to 3p$ DCS, does have structure at several of the excitation thresholds, although the scale of these are too small to be seen in Fig. 22(a). Most striking about this dipole-allowed cross section is the strong forward peaking which, as the energy increases, becomes more pronounced and shifts to smaller angles. Similar forward peaking is apparent in the corresponding optically allowed $|\Delta M_S|=0, |\Delta M_L|=1$ cross section $\sigma_1^0(\theta)$, but this phenomenon is considerably smaller than in $\sigma_0^0(\theta)$, as we expect from the Percival-Seaton threshold condition [102]

$$\lim_{E\to\epsilon_{ep}} \frac{\sigma_0^0(\theta)}{\sigma_1^0(\theta)} \to \infty \; . \qquad (4.6)$$

This cross section plunges to zero in the forward and backward directions, vivifying the quantal counterpart of the classical adage that angular momentum cannot be transferred in a straight-line collision.

The two cross sections for $|\Delta M_S|=1$ in Figs. 22(c) and 22(d) are less amenable to classical explanations since they are largely controlled by purely quantal exchange effects. Both $\sigma_0^1(\theta)$ and $\sigma_1^1(\theta)$ exhibit opulent structures between threshold and 4.6 eV, clustering at the myriad thresholds in this energy range. The DCS for $|\Delta M_L|=0$ in Fig. 22(c) exhibits pronounced backward peaking at energies below a few eV—a manifestation of the especial effectiveness of exchange at angles of greatest overlap of the projectile and core wave functions. The abrupt decrease of $\sigma_0^1(\theta)$ above about 3.5 eV is consistent with the diminished importance of exchange effects with increasing energy. [Because of the comparatively structureless character of $\sigma_0^1(\theta)$ above 4.5 eV, we do not show this energy range in Fig. 22.] Finally, the small but fascinating $\sigma_1^1(\theta)$ in Fig. 22(d) shows rich structure at low energies and the predominance of forward scattering at higher energies expected of a dipole-allowed excitation.

Let us now return to the experimental energies. In Fig. 23 we compare the results of Han, Schinn, and Gallagher for $\sigma_0^0(\theta)$, $\sigma_0^1(\theta)$, and $\sigma_1^0(\theta)$ to cross sections from 4CC, 7CC, and 10CC calculations. [No experimental results are available for $\sigma_1^1(\theta)$, as for this case the line shape cannot be extracted reliably from the experimental signal.] The first point to note is the excellent convergence at all three energies. Even $\sigma_1^1(\theta)$ is converged in the 7CC calculations except at the highest energy, where the $n=5$ states of the 10CC results affect details of its shape. Turning to the other, larger cross sections, we see in Fig. 23 that at 2.6 eV four states reproduce the oscillatory structure of $\sigma_0^0(\theta)$ as well as the more gentle undulations of $\sigma_0^1(\theta)$ and $\sigma_1^0(\theta)$. These shape characteristics are also evident at 3.1 and 3.6 eV. At these higher energies the $n=4, l>0$ states in the 7CC calculations are required to pin them down; but only at 3.6 eV do the $5p$ and $5d$ states in the 10CC calculations alter in the least the shapes of these cross sections.

The experimental $\sigma_0^0(\theta)$ at 2.6 eV does not show the backward peak or the intermediate-angle oscillations evident in the theoretical result. This difference is probably due to the fitting procedure used by Han, Schinn, and Gallagher, which does not allow for a peak in both the forward and backward directions, and which is

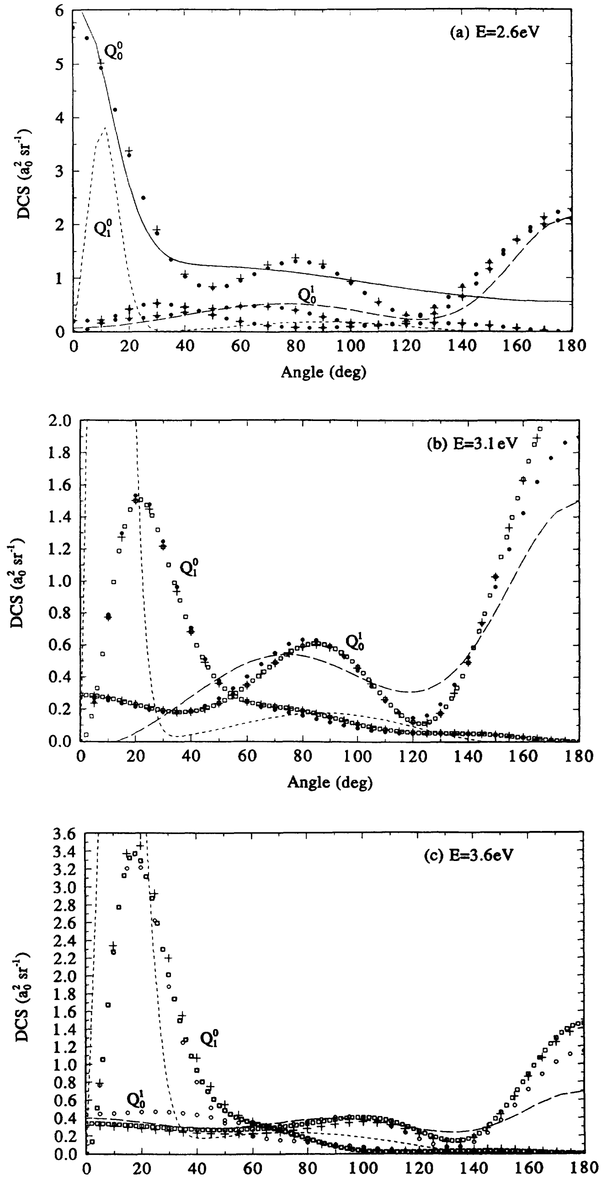

FIG. 23. Differential $3s\to 3p$ angular-momentum-changing cross sections compared to experimental data of Han, Schinn, and Gallagher (Ref. [117]) at (a) 2.6, (b) 3.1, and (c) 3.6 eV. The experimental data for $\sigma_0^0$ is represented by solid lines, $\sigma_0^1$ by long-dashed lines, and $\sigma_1^0$ by short-dashed lines. The theoretical results are from 7CC (pluses) and 4CC (closed circles), and, in (b) and (c), 10CC (open squares) $R$-matrix calculations.

insufficiently sensitive to detect variations where the DCS is small. Other differences in these figures are real, not artifacts of the fitting procedure. Thus at all three energies, the experimental $\sigma_1^0(\theta)$, for which only $M_L$ changes, is more strongly peaked than the theoretical result. The experimental $\sigma_0^1(\theta)$, for which only $M_S$ changes, is less strongly peaked in the backward direction.

The present theoretical calculations extend the experimental work of Han, Schinn, and Gallagher, which emphasized the near-threshold region, to energies up to 8.6 eV. Notwithstanding the dominance of $\sigma_0^0(\theta)$ for the $3s \rightarrow 3p$ transition, the theoretical angular-momentum-changing cross sections clarify and emphasize, as do the experiments of Han, Schinn, and Gallagher, the dominance of the exchange interactions for this important excitation.

### E. Polarization of the fluorescence from decay of the 3p state

To conclude this section we consider briefly the polarization of the atomic line radiation emitted in the decay of the electron-excited (unresolved) resonance doublet (the 3*p* state). A number of groups have measured this quantity [19,18,11,20,14,21], which is particularly interesting near threshold, where it reveals the influence of exchange.

If the target atoms are not polarized, the wave function is cylindrically symmetric with respect to the incident axis. Consequently the emitted photons are linearly polarized. Jitschin *et al.* [21] have measured the polarization of such photons in experiments involving spin-polarized atoms, where the degree of circular polarization provides insight into the importance of exchange for the $3s \rightarrow 3p$ excitation. These authors note that within experimental uncertainty the *linear* polarization of the fluorescence in their experiments is the same as that for unpolarized target atoms, the case of interest here, and it is to that data that we compare.

The linear polarization $P_{3p}$ reflects the anisotropy of the 3*p* state due to the collision. Hence it can be expressed in terms of the angular-momentum-changing cross sections of Sec. IV D. Since measurements of $P_{3p}$ do not entail spin analysis, we must first construct (integrated) cross sections for orbital angular momentum transfer $|\Delta M_L|$ as

$$\sigma_{|\Delta M_L|}(\theta) \equiv \sigma^0_{|\Delta M_L|}(\theta) + \sigma^1_{|\Delta M_L|}(\theta) \ . \tag{4.7}$$

From these partial cross sections, where $|\Delta M_L| = 0$ and 1, the percent polarization perpendicular to the incident electron wave vector for a $p \rightarrow s$ transition is [22]

$$P_{3p} = \frac{300(9\alpha_{\rm hfs} - 2)(\sigma_0 - \sigma_1)}{12(\sigma_0 + 2\sigma_1) + (9\alpha_{\rm hfs} - 2)(\sigma_0 - \sigma_1)} \ , \tag{4.8}$$

where $\alpha_{\rm hfs}$ is a constant that depends on the ratio of the hyperfine splitting in the exit channel (which diminishes the observable polarization) to the neutral linewidth; its value for Na is $\alpha_{\rm hfs} = 0.288$.

The values of $P_{3p}$ are compared to a variety of experimental determinations in Fig. 24. We first note seven target states is sufficient to converge this quantity except above about 5.0 eV, where one needs ten. Second, we note a satisfying confirmation of these calculations: as the exit-channel energy of the electron approaches zero at threshold, $P_{3p}$ approaches the theoretical limit for *e*-Na $P_{3p} = 14.104$ predicted by (4.8) for an excitation dominated by an outgoing *s* wave ($\sigma_1/\sigma_0 \rightarrow 0$ at $\epsilon_{3p}$ in Fig. 21). Thus the calculated results are consistent with fundamental, dynamics-independent threshold laws. Finally, we note that the theoretical values reveal near-threshold structures not seen in the experimental data.

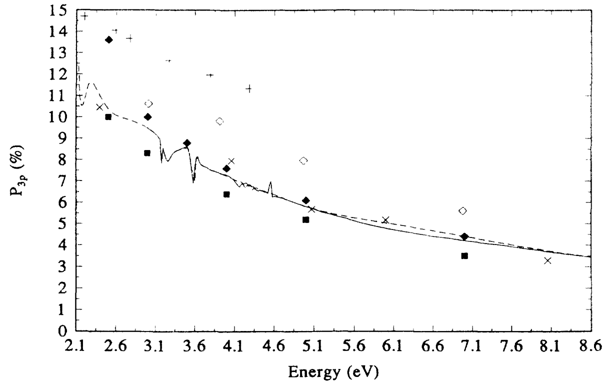

FIG. 24. Polarization of the fluorescence from decay of the 3*p* state emitted at 90° to the incident electron wave vector: theoretical 10CC (solid curve) and 7CC (dashed curves) values and experimental data of Enemark and Gallagher (Ref. [11]) (closed squares), Gould (Ref. [18]) (crosses), Hafner and Kleinpoppen (Ref. [19]) (pluses), Jitschin *et al.* (Ref. [21]) (open diamonds), and Phelps and Lin (Ref. [14]) (closed diamonds).

## V. CONCLUSION

The present theoretical study of *e*-Na collisions is the most comprehensive look to date at low-energy scattering from the ground state of an alkali-metal atom. Based on close-coupling *R*-matrix calculations within the *LS*-coupling representation appropriate to this low-*Z* target, the various scattering quantities reported here, converged in the space of bound target states and in partial waves, are approximate primarily in their representation of core and dielectronic polarization. Overall, the comparisons in this paper to experiment and other theory indicate the accuracy of these approximations for integrated and differential elastic and inelastic cross sections at energies below about 8 eV, and suggest their viability for more complicated systems for which, say, optical-potential calculations may be technically infeasible or excessively expensive. The accuracy of the present approach hinges in part on the validity of neglecting explicit inclusion of the continuum for the energy range of interest; as discussed in Sec. IV A 4, comparison to recent CCO calculations show this approximation to be valid for *e*-Na scattering at energies below 8.6 eV.

The present study of elastic scattering and excitation of the 3*p*, 4*s*, 3*d*, and 4*p* excited states has uncovered a wealth of structures at each of the excited-state thresholds. By decomposing these cross sections into singlet and triplet contributions (and, in some cases, further into partial-wave contributions) we have gained insight into the origin of these structures. This decomposition has also shown how various spin channels control each cross section as the scattering energy changes. In particular we have investigated in detail the well-known cusp in the elastic DCS at the $3p$ threshold and less well-known features near the $3d$ threshold. And our investigation of various inelastic cross sections near their respective inelastic thresholds has confirmed [16] that the onsets of $\sigma_{3s\rightarrow 3d}$ and $\sigma_{3s\rightarrow 4s}$ are much more rapid than that of $\sigma_{3s\rightarrow 4p}$.

Comparison of our converged cross sections to experimental results for these excitations has shown that some of these results may not be as accurate as heretofore thought; in particular we have been able to address concerns expressed in several prior reports that differences between experiment and theory (previously the 4CC results of Moores and Norcross) might have been due to lack of convergence. Instead, we find for the important $3s\rightarrow 3p$ transition that our converged cross sections, which at higher energies do require inclusion of states with $n=4$, $l>0$, and $n=5$, differ strikingly from many current measured cross sections. Such findings argue for a reconsideration of measurements of these low-lying $e$-Na cross sections. The present three-dimensional graphs of various DCS reveal the overall structure of these cross sections and suggest angular and energy ranges for such measurements. Finally, our converged angular-momentum-changing differential cross sections $\sigma^{|\Delta M_S|}_{|\Delta M_L|}(\theta)$ provide detailed information concerning their angular and energy dependence that should be of value to future experimental studies of exchange interactions in low-energy electron–alkali-metal-atom scattering.

In this paper we have considered only scattering of unpolarized electrons from the ground state of unpolarized atoms. Future papers in this series will explore scattering from excited states and collisions involving polarized targets and/or projectiles.

## ACKNOWLEDGMENTS

We would like to thank Dr. Eric Layton for invaluable conversations concerning various aspects of this research and to acknowledge Dr. Werner Eisner and Dr. Kenneth Bell for providing improved unpublished versions of the $R$ matrix and asymptotic codes. We would also like to thank Dr. Lepsa Vušković for sending us her measured elastic and inelastic DCS, Dr. Igor Bray for making available results of his coupled-channel optical calculations prior to publication, and Dr. Alan Gallagher and Dr. Chris Greene for valuable suggestions that improved the present manuscript. Three of us (M.A.M., K.B.M., and K.B) would also like to thank the Joint Institute for Laboratory Astrophysics, for hospitality during the period that most of this work was completed. This work used the Cray facilities at NIST (Gaithersburg, MD), NERSC (Livermore, CA), and NCSA (San Diego, CA). M.A.M. gratefully acknowledges the support of the National Science Foundation under Grant No. PHY-9108890, as does K.B.M. under Grant No. PHY-9122377 and K.B. under Grant No. PHY-9014103. Finally W.K.T. and D.W.N. would like to acknowledge partial support by NSF Grant No. PHY-9012244.

---

[1] D. L. Moores and D. W. Norcross, J. Phys. B **5**, 1482 (1972).

[2] For a review of experimental work prior to 1970, see B. L. Moiseiwitsch and S. J. Smith, Rev. Mod. Phys. **40**, 238 (1968).

[3] B. L. Moiseiwitsch and S. J. Smith, Rev. Mod. Phys. **41**, 574 (1969).

[4] For the period from 1968 through 1977, see B. H. Bransden and M. R. C. McDowell, Phys. Rep. **3**, 207 (1977).

[5] B. H. Bransden and M. R. C. McDowell, Phys. Rep. **7**, 249 (1978).

[6] W. Gehenn and E. Reichert, Z. Phys. **254**, 28 (1972).

[7] D. Andrick, M. Eyb, and H. Hofmann, J. Phys. B **5**, L15 (1972).

[8] H. Hafner, Phys. Lett. **43A**, 265 (1973).

[9] M. Eyb and H. Hofmann, J. Phys. B **8**, 1095 (1975).

[10] M. Zuo, T. Y. Jiang, L. Vušković, and B. Bederson, Phys. Rev. A **41**, 2489 (1990).

[11] E. A. Enemark and A. Gallagher, Phys. Rev. A **6**, 192 (1972).

[12] A. Kasdan, T. M. Miller, and B. Bederson, Phys. Rev. A **8**, 1562 (1973).

[13] I. P. Zapesochnyĭ, E. N. Postoĭ, and I. S. Aleksakhin, Zh. Eksp. Teor. Fiz. **68**, 1724 (1975) [Sov. Phys. JETP **41**, 865 (1975)].

[14] J. O. Phelps and C. C. Lin, Phys. Rev. A **24**, 1299 (1981).

[15] B. Stumpf and A. Gallagher, Phys. Rev. A **32**, 3344 (1985).

[16] B. Marinković, P. Wang, and A. Gallagher, Phys. Rev. A **46**, 2553 (1992).

[17] C. K. Kwan, W. E. Kaupilla, R. A. Lukaszew, S. P. Parikh, T. S. Stein, Y. J. Wan, and M. S. Dababneh, Phys. Rev. A **44**, 1620 (1991).

[18] G. N. Gould, Ph.D. thesis, University of New South Wales, 1970 (unpublished).

[19] H. Hafner and H. Kleinpoppen, Z. Phys. D **198**, 315 (1967).

[20] B. Stumpf, K. Becker, and G. Schulz, J. Phys. B **11**, 1639 (1978).

[21] W. Jitschin, S. Osimitsch, H. Reihl, H. Kleinpoppen, and H. O. Lutz, J. Phys. B **17**, 1899 (1984).

[22] D. R. Flower and M. J. Seaton, Proc. Phys. Soc. **91**, 59 (1967).

[23] J. Kessler, Comments At. Mol. Phys. **17**, 15 (1985).

[24] J. Kessler, *Polarized Electrons*, 2nd ed. (Springer-Verlag, Berlin, 1985).

[25] J. Kessler, Adv. At. Mol. Phys. **27**, 81 (1991).

[26] G. Hanne, in *Proceedings of the Seventeenth International Conference on the Physics of Electronic and Atomic Collisions*, edited by W. R. MacGillivray, I. E. McCarthy, and M. C. Standage (Hilger, New York, 1992), p. 199.

[27] J. J. McClelland, M. H. Kelley, and R. J. Celotta, Phys. Rev. Lett. **55**, 688 (1985).

[28] J. J. McClelland, M. H. Kelley, and R. J. Celotta, Phys.

Rev. Lett. **56**, 1362 (1986).

[29] J. J. McClelland, M. H. Kelley, and R. J. Celotta, J. Phys. B **20**, L385 (1987).

[30] J. J. McClelland, M. H. Kelley, and R. J. Celotta, Phys. Rev. A **40**, 2321 (1989).

[31] V. Nickich, T. Hegemann, M. Bartsch, and G. F. Hanne, Z. Phys. D **16**, 261 (1990).

[32] R. E. Scholten, S. R. Lorentz, J. J. McClelland, M. H. Kelley, and R. J. Celotta, J. Phys. B **24**, L653 (1991).

[33] T. Y. Jiang, M. Zou, L. Vušković, and B. Bederson, Phys. Rev. Lett. **68**, 915 (1992).

[34] J. J. McClelland, S. R. Lorentz, R. E. Scholten, M. H. Kelley, and R. J. Celotta, Phys. Rev. A **46**, 6079 (1992).

[35] N. Andersen and K. Bartschat, Phys. Rev. A (to be published).

[36] T. Hegemann, M. Oberste-Vorth, R. Vogts, and G. F. Hanne, Phys. Rev. Lett. **66**, 2968 (1991).

[37] H. W. Hermann, I. V. Hertel, W. Reiland, A. Stamatović, and W. Stoll, J. Phys. B **10**, 251 (1977).

[38] B. Jaduszliwer, R. Dang, P. Weiss, and B. Bederson, Phys. Rev. A **21**, 808 (1990).

[39] B. Jaduszliwer, G. F. Shen, J.-L. Cai, and B. Bederson, Phys. Rev. A **31**, 1157 (1985).

[40] H. W. Hermann, I. V. Hertel, and M. H. Kelley, J. Phys. B **13**, 3465 (1980).

[41] H. W. Hermann and I. V. Hertel, Z. Phys. A **307**, 89 (1982).

[42] I. V. Hertel, M. H. Kelley, and J. J. McClelland, Z. Phys. D **6**, 163 (1987).

[43] H. Kleinpoppen, Phys. Rev. A **3**, 2015 (1971).

[44] N. Andersen, J. W. Gallagher, and I. V. Hertel, Phys. Rep. **165**, 1 (1988).

[45] H. W. Hermann and I. V. Hertel, in *Coherence and Correlation in Atomic Collisions*, edited by H. Kleinpoppen and J. F. Williams (Plenum, New York, 1980), p. 50.

[46] H. Kleinpoppen, Adv. At. Mol. Phys. **15**, 423 (1979).

[47] N. Andersen and S. L. Nielsen, Adv. At. Mol. Phys. **18**, 265 (1982).

[48] I. V. Hertel and W. Stoll, Adv. At. Mol. Phys. **13**, 113 (1977).

[49] D. L. Moores, D. W. Norcross, and V. B. Sheorey, J. Phys. B **7**, 371 (1974).

[50] B. Bederson, Comments At. Mol. Phys. **1**, 41 (1969); **1**, 65 (1969).

[51] P. G. Burke and J. F. B. Mitchell, J. Phys. B **7**, 665 (1973).

[52] M. Weissbluth, *Atoms and Molecules* (Academic, New York, 1978), p. 409.

[53] J. Mitroy and D. W. Norcross, Phys. Rev. A **37**, 3755 (1988).

[54] E. Clementi and C. Roetti, At. Data. Nucl. Data Tables **14**, 177 (1974).

[55] H. L. Zhou, B. L. Whitten, G. Snitchler, D. W. Norcross, and J. Mitroy, Phys. Rev. A **42**, 3907 (1990).

[56] J. Mitroy (private communication).

[57] K. A. Berrington, P. G. Burke, M. LeDourneuf, W. D. Robb, K. T. Taylor, and Vo Ky Lan, Comput. Phys. Commun. **14**, 367 (1978).

[58] K. A. Berrington, P. G. Burke, J. J. Chang, A. T. Chivers, W. D. Robb, and K. T. Taylor, Comput. Phys. Commun. **8**, 149 (1974).

[59] N. S. Scott and K. T. Taylor, Comput. Phys. Commun. **25**, 347 (1982).

[60] D. W. Norcross, J. Phys. B **4**, 1458 (1971).

[61] J. C. Stewart and M. Rotenberg, Phys. Rev. A **140**, 1508 (1965).

[62] I. Bray, A. Konovalov, and I. E. McCarthy, Phys. Rev. A **44**, 7830 (1991).

[63] P. Risberg, Ark. Fys. **10**, 583 (1965).

[64] L. Castillejo, I. C. Percival, and M. J. Seaton, Proc. R. Soc. London, Ser. A **254**, 259 (1960).

[65] M. J. Seaton and L. Steenman-Clark, J. Phys. B **10**, 2639 (1977); **11**, 293 (1978).

[66] J. Callaway, R. W. LaBahn, R. T. Pu, and W. M. Duxler, Phys. Rev. **168**, 12 (1968).

[67] C. E. Moore, Natl. Bur. Stand. Ref. Data Ser., Natl. Bur. Stand. (U.S.) Circ. No. 467 (U.S. GPO, Washington, D.C., 1949), Vol. 1.

[68] D. W. Norcross, Phys. Rev. Lett. **32**, 192 (1974).

[69] S. Hameed, A. Herzenberg, and M. G. James, J. Phys. B **2**, 822 (1968).

[70] G. A. Victor and C. Laughlin, Chem. Phys. Lett. **14**, 74 (1972).

[71] U. Thumm and D. W. Norcross, Phys. Rev. A **45**, 6349 (1992).

[72] D. W. Norcross and M. J. Seaton, J. Phys. B **17**, 1983 (1976).

[73] H. Reeh, Z. Naturforsch. **15A**, 377 (1960).

[74] C. D. H. Chrisholm and U. Öpik, Proc. Phys. Soc. **83**, 541 (1964).

[75] H. Eissa and U. Öpik, Proc. Phys. Soc. **92**, 556 (1967).

[76] C. Bottcher and A. Dalgarno, Proc. R. Soc. London, Ser. A **341**, 187 (1974).

[77] We use lower-case symbols for quantum numbers of individual electrons (e.g., $m_s$ for the projection of the spin of the scattering electron on the quantization axis), capital letters for quantum numbers of the $N_e$-electron states of the target (e.g., $M_L$ for the projection of the total orbital angular momentum), and script capital letters for quantum numbers of the *e*-Na system (e.g., $\mathcal{L}$ for the total orbital angular momentum).

[78] P. G. Burke, A. Hibbert, and W. D. Robb, J. Phys. B **4**, 153 (1971).

[79] R. G. Newton, *Scattering Theory of Waves and Particles*, 2nd ed. (Springer-Verlag, New York, 1982).

[80] J. Mitroy, I. E. McCarthy, and A. T. Stelbovics, J. Phys. B **20**, 4827 (1987).

[81] A. Z. Msezane, Phys. Rev. A **37**, 1787 (1988).

[82] D. H. Oza, Phys. Rev. A **37**, 2721 (1988).

[83] A. Z. Msezane, C. R. Handy, G. Mantica, and J. Lee, Phys. Rev. A **38**, 1604 (1988).

[84] D. H. Madison, K. Bartschat, and R. P. McEachran, J. Phys. B **25**, 5119 (1992).

[85] E. P. Wigner and L. Eisenbud, Phys. Rev. **72**, 29 (1947).

[86] P. G. Burke and W. D. Robb, Adv. At. Mol. Phys. **11**, 143 (1975).

[87] P. G. Burke, Comput. Phys. Commun. **6**, 288 (1974).

[88] N. F. Lane, Rev. Mod. Phys. **52**, 29 (1980).

[89] P. G. Burke and W. Eisner, in *Atoms in Astrophysics*, edited by P. G. Burke *et al.* (Plenum, New York, 1983).

[90] All of our calculations were performed using computer packages originally developed by the Belfast Group (see, for example, Ref. [89]) with local modifications to incorporate the treatment of core polarization described in Sec. III B.

[91] Hsiao-Ling Zhou, Ph.D. thesis, University of Colorado, 1991.

[92] In practice we chose the value of $r_b$ by examining the wave function of the most diffuse bound orbital. We re-

quire the value of this function at $r=r_b$ be 0.1% of its peak value.

[93] Throughout this section overbars denote quantities defined within the $R$-matrix box that satisfy these boundary conditions.

[94] C. Bloch, Nucl. Phys. **4**, 503 (1957), translation available from the Los Alamos National Laboratory Report No. LA-UR-76-10.

[95] P. J. A. Buttle, Phys. Rev. **160**, 719 (1967).

[96] M. J. Seaton, Proc. R. Soc. London, Ser. A **77**, 174 (1961); **77**, 174 (1961).

[97] J. Lawson, W. Lawson, and M. J. Seaton, Proc. R. Soc. London, Ser. A **77**, 174 (1961).

[98] D. W. Norcross, Comput. Phys. Commun. **1**, 88 (1969).

[99] D. W. Norcross, Comput. Phys. Commun. **6**, 257 (1974).

[100] D. W. Norcross, in *Atoms in Astrophysics* (Ref. [89]).

[101] J. P. Croskery, N. S. Scott, K. L. Bell, and K. A. Berrington, Comput. Phys. Commun. **27**, 1856 (1982); K. L. Bell (private communication).

[102] I. C. Percival and M. J. Seaton, Philos. Trans. R. Soc. London A **251**, 113 (1958).

[103] Here and in several other graphs of cross sections, we have chosen limits on the horizontal axes so as to emphasize regions of complicated variation and structure; hence the vertical axis on most of these graphs do not start at zero.

[104] In all graphs of singlet and triplet cross sections we show values weighted by the statistical spin-degeneracy factors $\frac{1}{4}$ for singlet and $\frac{3}{4}$ for triplet cross sections.

[105] M. A. Morrison, W. K. Trail, and T. L. Goforth (unpublished).

[106] I. Bray (private communication).

[107] I. Bray and I. E. McCarthy, Phys. Rev. A **47**, 317 (1993).

[108] I. E. McCarthy, Comments At. Mol. Phys. **24**, 343 (1990).

[109] I. E. McCarthy and E. Weigold, Adv. At. Mol. Phys. **77**, 165 (1991).

[110] I. Bray, in Ref. [26], p. 191.

[111] I. Bray, D. A. Konovalov, and I. E. McCarthy, Phys. Rev. A **44**, 7179 (1991).

[112] The results quoted in this paper for 1.0 and 1.6 eV are from 15-state coupled-channel calculations without the optical potential; those at 4.1 eV are from calculations using the full CCO method.

[113] I. E. McCarthy and A. T. Stelbovics, Phys. Rev. A **28**, 2693 (1983).

[114] N. F. Mott and H. S. W. Massey, *The Theory of Atomic Collisions* (Clarendon, Oxford, 1971).

[115] E. Wigner, Phys. Rev. **73**, 1002 (1948).

[116] X. L. Han, G. W. Schinn, and A. Gallagher, Phys. Rev. A **38**, 535 (1988).

[117] X. L. Han, G. W. Schinn, and A. Gallagher, Phys. Rev. A **42**, 1245 (1990).

[118] H. Friedrich, *Theoretical Atomic Physics* (Springer-Verlag, New York, 1991).

[119] C. H. Ying, F. Perales, L. Vušković, and B. Bederson, Phys. Rev. A **48**, 1189 (1993).

[120] L. Vušković (private communication).

(a) 3s→3p

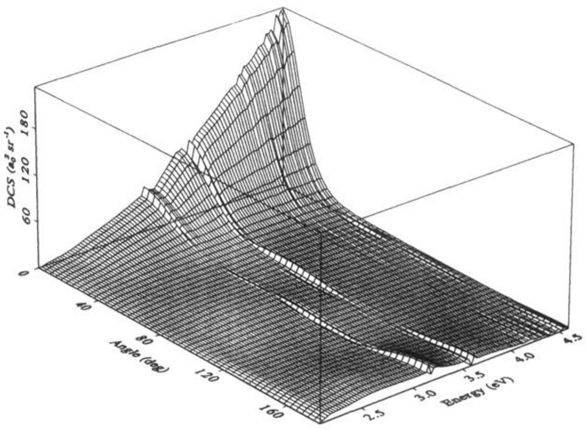

(b) 3s→4s

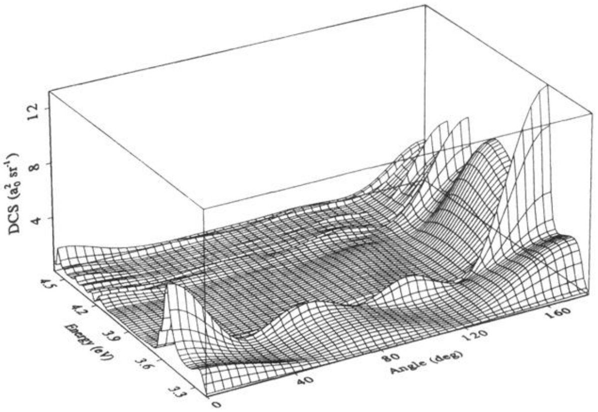

**FIG. 20.** Three-dimensional overview of the (a) $3s \rightarrow 3p$ and (b) $3s \rightarrow 4s$ inelastic $e$-Na differential cross sections.

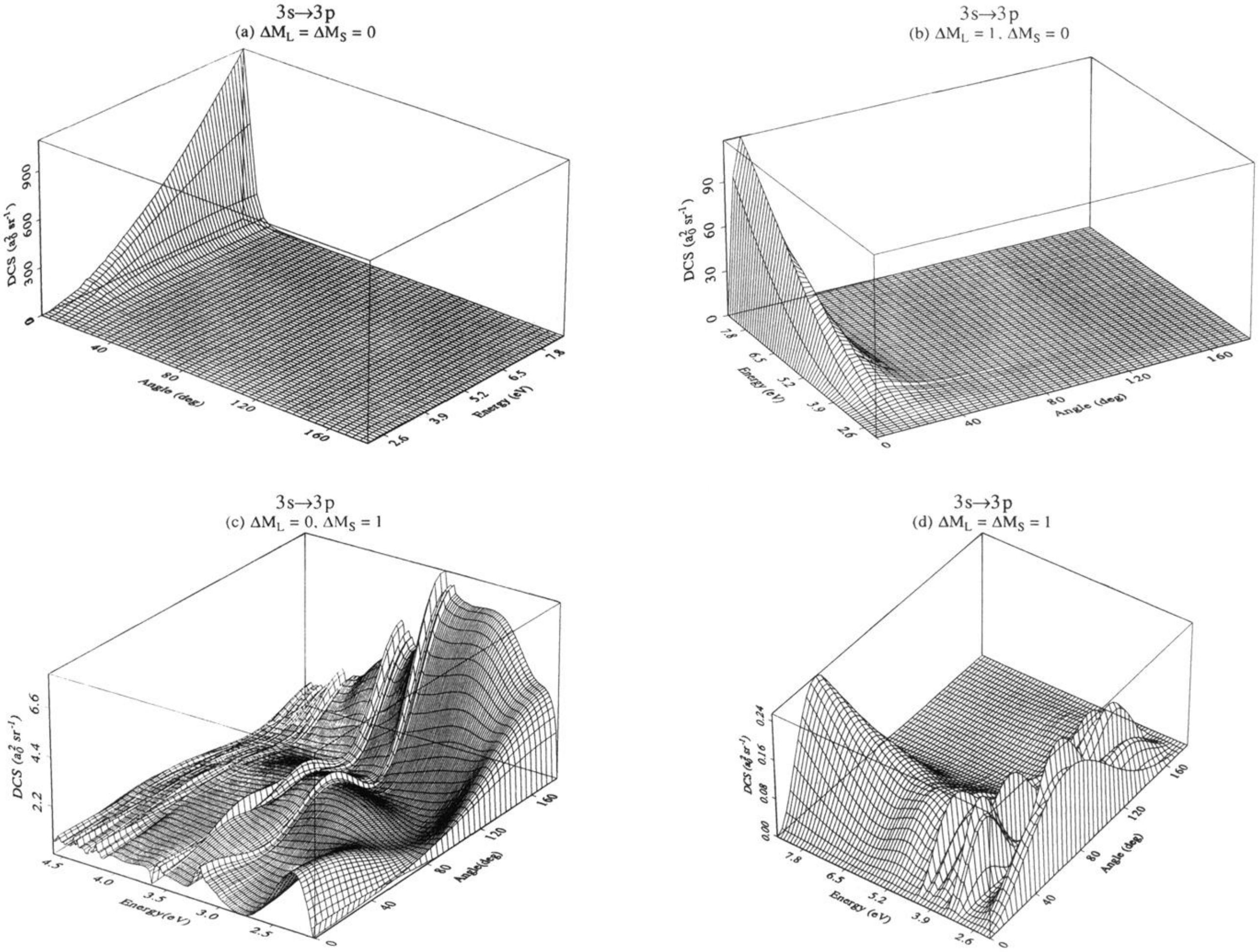

**FIG. 22. Energy and angular dependence of the four independent angular-momentum-changing differential $3s \rightarrow 3p$ cross sections for *e*-Na scattering: (a) $\sigma_0^0(\theta)$, (b) $\sigma_1^0(\theta)$, (d) $\sigma_0^1(\theta)$, and (d) $\sigma_1^1(\theta)$.**